iScience

CellPress
OPEN ACCESS

Article

Transcriptomic profiling of SARS-CoV-2 infected human cell lines identifies HSP90 as target for COVID-19 therapy

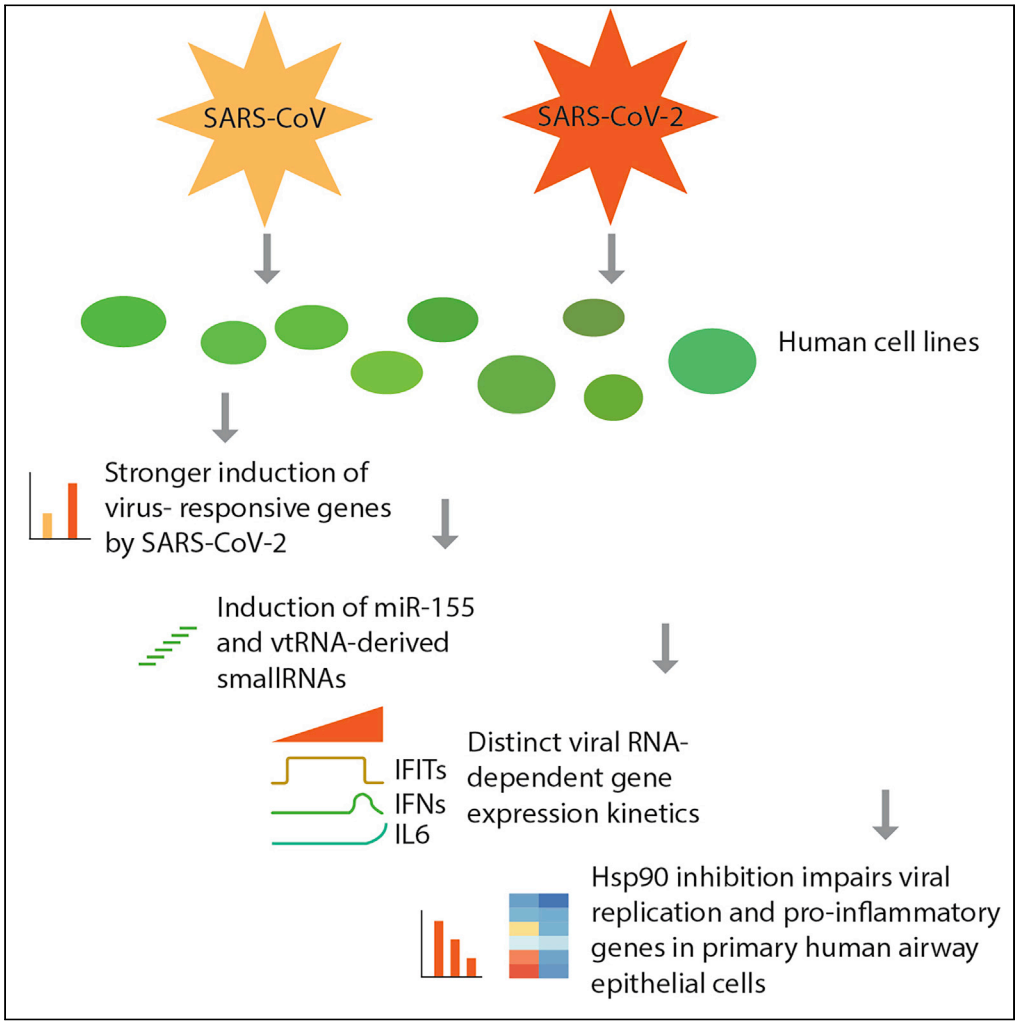

Emanuel Wyler, Kirstin Mösbauer, Vedran Franke, ..., Nikolaus Rajewsky, Christian Drosten, Markus Landthaler

emanuel.wyler@mdc-berlin.de (E.W.)
christian.drosten@charite.de (C.D.)
markus.landthaler@mdc-berlin.de (M.L.)

HIGHLIGHTS

Transcriptomic landscape of human cell lines infected with SARS-CoV or SARS-CoV-2

Stronger innate immune response to SARS-CoV-2 and induction of miR-155

Transcription of interferon gene is transient and followed by NF-kB target genes

Hsp90 inhibitors impair viral replication and induction of pro-inflammatory genes

Wyler et al., iScience 24, 102151
March 19, 2021
https://doi.org/10.1016/j.isci.2021.102151

iScience

CellPress
OPEN ACCESS

Article

Transcriptomic profiling of SARS-CoV-2 infected human cell lines identifies HSP90 as target for COVID-19 therapy

Emanuel Wyler,[1,9,*] Kirstin Mösbauer,[2,9] Vedran Franke,[1,9] Asija Diag,[1] Lina Theresa Gottula,[2] Roberto Arsiè,[1] Filippos Klironomos,[1,4] David Koppstein,[1] Katja Hönzke,[5] Salah Ayoub,[1] Christopher Buccitelli,[3] Karen Hoffmann,[5] Anja Richter,[2] Ivano Legnini,[1] Andranik Ivanov,[6] Tommaso Mari,[3] Simone Del Giudice,[1] Jan Papies,[2] Samantha Praktiknjo,[1] Thomas F. Meyer,[7] Marcel Alexander Müller,[2] Daniela Niemeyer,[2] Andreas Hocke,[5] Matthias Selbach,[3] Altuna Akalin,[1] Nikolaus Rajewsky,[1] Christian Drosten,[2,*] and Markus Landthaler[1,8,10,*]

SUMMARY

Detailed knowledge of the molecular biology of severe acute respiratory syndrome coronavirus 2 (SARS-CoV-2) infection is crucial for understanding of viral replication, host responses, and disease progression. Here, we report gene expression profiles of three SARS-CoV- and SARS-CoV-2-infected human cell lines. SARS-CoV-2 elicited an approximately two-fold higher stimulation of the innate immune response compared to SARS-CoV in the human epithelial cell line Calu-3, including induction of miRNA-155. Single-cell RNA sequencing of infected cells showed that genes induced by virus infections were broadly upregulated, whereas interferon beta/lambda genes, a pro-inflammatory cytokines such as IL-6, were expressed only in small subsets of infected cells. Temporal analysis suggested that transcriptional activities of interferon regulatory factors precede those of nuclear factor κB. Lastly, we identified heat shock protein 90 (HSP90) as a protein relevant for the infection. Inhibition of the HSP90 activity resulted in a reduction of viral replication and pro-inflammatory cytokine expression in primary human airway epithelial cells.

INTRODUCTION

Diseases caused by coronaviruses (CoVs) range from asymptomatic and mild infections of the upper respiratory tract to severe acute respiratory distress, when the lower respiratory tract is infected. In addition to the six previously known CoVs affecting humans, a novel CoV termed severe acute respiratory syndrome coronavirus 2 (SARS-CoV-2) has recently emerged. The novel SARS-CoV-2, which causes coronavirus disease 2019 (COVID-19), is an ongoing global health threat since the beginning of the outbreak in late 2019 and has, at the time of writing this text, infected more than 80 million people worldwide (World Health Organization, 2020). The SARS-CoV-2 life cycle initiates with the attachment of the virion to the cell surface and subsequent binding to the angiotensin converting enzyme 2 (ACE2), followed by proteolytic cleavage and internalization (Fehr and Perlman, 2015; Hoffmann et al., 2020; Masters and Perlman, 2013). Non-structural proteins are then translated to form a replicase-transcriptase complex, in which the full genomic RNA, as well as subgenomic RNAs are generated within double membrane vesicles (DMVs) (Fehr and Perlman, 2015; Masters and Perlman, 2013; van Hemert et al., 2008). Incoming viral RNA is detected by sensors such as IFIH1 (interferon induced with helicase C domain 1; also known as MDA5) and DDX58 (DExD/H-Box helicase 58; also known as RIG-I), which trigger the antiviral response. This sensing and signaling is impaired by a range of viral factors, e.g. replication within DMVs, RNA capping, and methylation, or shortening of the poly-U tail on the minus strand RNA (Hackbart et al., 2020; Menachery et al., 2014a). Furthermore, inhibition of interferon regulatory factor (IRF) activity (Spiegel et al., 2005) and a delayed induction of interferon-stimulated genes (ISGs) compared to influenza virus infection or type I interferon treatment itself (Menachery et al., 2014b) was observed in SARS-CoV infection. Importantly, accessory genes in the SARS-CoV genome, like open reading frame 6 (ORF6), may code for antagonists of interferon signaling (Narayanan et al., 2008).

[1]Berlin Institute for Medical Systems Biology, Max-Delbrück-Center for Molecular Medicine in the Helmholtz Association, Hannoversche Str 28, 10115 Berlin, Germany

[2]Institute of Virology, Charité-Universitätsmedizin Berlin and Berlin Institute of Health, Charitéplatz 1, 10117 Berlin, Germany

[3]Max-Delbrück-Center for Molecular Medicine in the Helmholtz Association, Robert-Rössle-Strasse 10, 13125 Berlin, Germany

[4]Department of Pediatrics, Charité – University Hospital Berlin, 13353 Berlin, Germany

[5]Department of Internal Medicine/Infectious Diseases and Pulmonary Medicine, Charité University Medicine, Berlin, Germany

[6]Core Unit Bioinformatics, Berlin Institute of Health, Charité – University Hospital Berlin, 10117 Berlin, Germany

[7]Laboratory of Infection Oncology, Institute of Clinical Molecular Biology, UKSH, Christian Albrechts University of Kiel, 24105 Kiel, Germany

[8]IRI Life Sciences, Institut für Biologie, Humboldt Universität zu Berlin, Philippstraße 13, 10115 Berlin, Germany

[9]These authors contributed equally

[10]Lead contact

*Correspondence: emanuel.wyler@mdc-berlin.de (E.W.), christian.drosten@charite.de (C.D.), markus.landthaler@mdc-berlin.de (M.L.)

https://doi.org/10.1016/j.isci.2021.102151

Following production of subgenomic RNAs, during which a constant 5′ leader is prepended by a process called discontinuous transcription (Sola et al., 2015), the viral genes are translated either in the cytoplasm, e.g. the nucleocapsid protein, N, or at the endoplasmic reticulum (ER), such as the envelope (E), membrane (M), and spike (S) proteins (Alsaadi and Jones, 2019; Muller et al., 2010). The substantial increase in ER translation causes ER stress, which triggers the unfolded protein response (UPR). This is then integrated with double-stranded RNA sensing at the level of eukaryotic initiation factor 2 alpha (eIF2alpha) phosphorylation (Fung and Liu, 2014). The ER stress response is likely attenuated by the viral E protein (DeDiego et al., 2011; Li et al., 2019). Accordingly, heat shock proteins (HSPs), which ameliorate ER stress, have been described to be generally relevant for virus infections (Santoro et al., 2010). Furthermore, ER stress induces autophagy, a cell recycling pathway which can be used by some viruses for productive replication (Guo et al., 2017). Finally, dysregulation of microRNA (miRNA) expression and subsequent alterations in gene expression patterns have also been reported to play a role in infected cells (Kemp et al., 2020; Leon-Icaza et al., 2019).

Comprehensive profiling of SARS-CoV-2-mediated perturbations of gene expression are at the beginning. A recent in-depth analysis of the transcriptional response to SARS-CoV-2 in comparison to other respiratory viruses in cells and animal models revealed a virus-specific inflammatory response (Blanco-Melo et al., 2020). For further in-depth studies, high-resolution methods such as single-cell RNA-sequencing (scRNA-seq) are of particular interest. They allow the characterization of cellular heterogeneity over the course of infection, which may be masked at the population level (Cristinelli and Ciuffi, 2018; Drayman et al., 2019; Russell et al., 2018; Shnayder et al., 2018; Wyler et al., 2019; Zanini et al., 2018). Furthermore, techniques such as small RNA sequencing, which reveals miRNAs and other small RNAs (Bartel, 2004; Friedlander et al., 2012), allow the characterization of other aspects influencing the regulation of gene expression.

Here, we performed a comprehensive analysis of three human cell lines infected with SARS-CoV or SARS-CoV-2, namely the gut cell line Caco-2, as well as the lung cell lines Calu-3 and H1299. We generated scRNA-seq, poly(A)$^+$, and total RNA transcriptomic data, as well as small RNA profiling in infection time courses for both viruses.

Efficiency and productivity of infection as well as the interferon response was remarkably different between cell lines. Interestingly, SARS-CoV-2 induced a two-fold higher expression of genes induced by the infection than SARS-CoV. In addition, we found strong induction of miR-155 with both viruses, suggesting a role for this miRNA in the progression of infection. The scRNA-seq data showed that while some genes such as interferon-induced protein with tetratricopeptide repeats 1 and 2 (IFIT1/IFIT2) were broadly induced, interferon beta (IFNB1) and interleukin-6 (IL6) were expressed only in subsets of infected cells. Furthermore, the transcriptional induction of nuclear factor-κB (NF-κB) targets could be temporally separated from the interferon-driven transcription. Detailed investigations of cellular gene expression programs suggest an involvement of the protein folding chaperone and autophagy regulator HSP90 in the viral infection cycle. Inhibition of HSP90 by multiple inhibitors resulted in reduced viral replication and cytokine mRNA levels. Overall, our study provides a detailed picture of the gene expression changes in cell line models for CoVs and particularly SARS-CoV-2, highlights the cell-type specificity of the transcriptional response to infection and identifies HSP90 as a potential target for therapeutic interventions.

RESULTS

Different permissiveness of SARS-CoV-2 infection in cell lines

To establish cell culture systems for studying SARS-CoV-2 replication and host cell responses, we examined the epithelial lung cancer cell lines, H1299 and Calu-3, since infection of lung epithelial cells is a key feature of SARS-CoV-2 infection in the human body. In addition, we used the epithelial colorectal adenocarcinoma cell line, Caco-2, which is frequently used as a CoV cell culture model (Bojkova et al., 2020; Chu et al., 2020; Klann et al., 2020; Reigel, 1985), and infection of intestinal cells is still under debate (Lamers et al., 2020). Transfection of poly-I:C RNA resulted in induction of IFIT1, IFIT2, and OAS2 (2′-5′-Oligoadenylate Synthetase 2) genes in Calu-3 and H1299 cells, indicating that sensing of foreign RNA in the cytosol is active in these cell types. This response was not observed in Caco-2 cells (Figure S1A), which exhibit low expression of viral RNA receptor genes, IFIH1/MDA5 and DDX58/RIG-I (Figure S2C).

For all cell lines, we performed a comprehensive analysis of transcriptome changes. Cells were infected with either SARS-CoV (Frankfurt strain) or SARS-CoV-2 (patient isolate BetaCoV/Munich/BavPat1/2020|EPI_ISL_406862) at

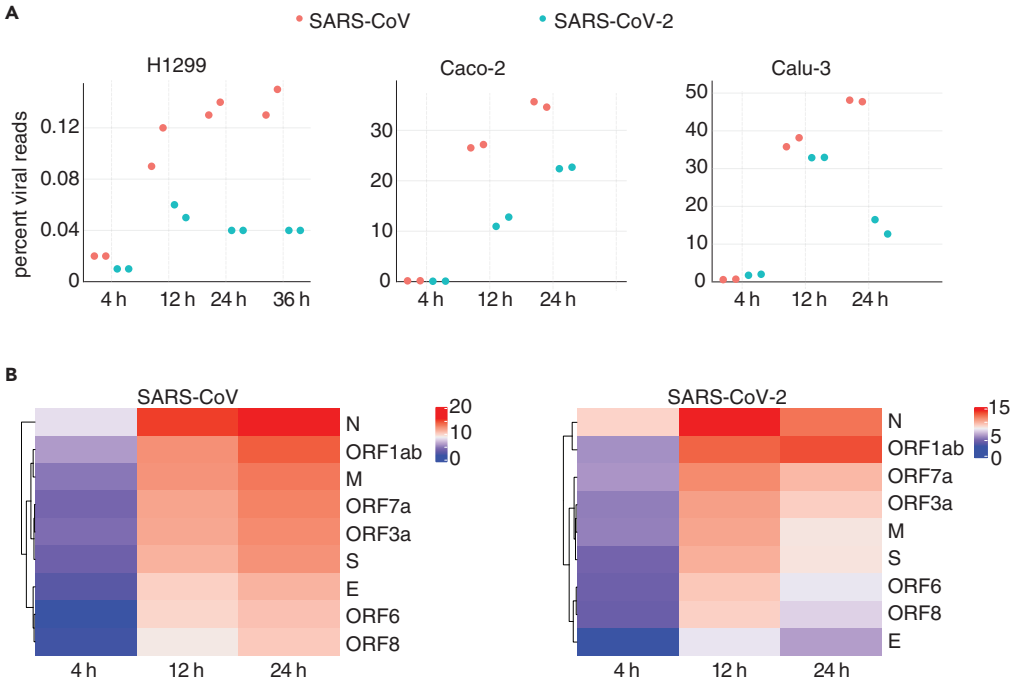

Figure 1. Different permissiveness of SARS-CoV/-2 infection in cell lines

(A) Viral read percentages of total reads of the respective cell line at different time points of infection. Note that Calu-3 cells infected with SARS-CoV-2 show clear signs of cell death at 24 hpi (Figure S1I), which likely influences the viral yield at the latest time point.

(B) Heatmaps of canonical junction-spanning viral reads in total RNA from Calu-3 cells infected with either virus, averaged across biological replicates per time point, expressed in $\log_2$(TMM-normalized counts per million).

an MOI of 0.33 (schematic representation of experiments in Figure S1B and Table S1), and sampled at different time points after infection. The percentages of viral transcripts in intracellular RNAs, as determined by poly(A)$^+$ and RNA-seq sequencing were low in H1299 cells for both viruses, in contrast to Caco-2 and Calu-3 cells (Figure 1A, Table S2). Accordingly, the yield of infectious virus particles was higher for the permissive cell lines Caco-2 and Calu-3 (Figure S1C). The low susceptibility of H1299 cells might, at least partially, be attributed to the low expression of the SARS-CoV receptor ACE2, as suggested by the RNA-sequencing data and Western blot analysis (Figure S1D).

By counting poly(A)$^+$ or total RNA-seq reads spanning the junction of the viral leader and its downstream gene (82.6% of virus-mapping split reads), we accurately quantified the relative amounts of subgenomic viral mRNAs (Irigoyen et al., 2016; Kim et al., 2020). We observed a consistent, time-dependent hierarchy of gene expression, mostly dominated by viral mRNAs encoding the N gene (Figures 1B and S1E–S1H), similar to a recent report for the alpha Human CoV-229E (HCoV-229E) (Viehweger et al., 2019). At later time points post infection, the relative amount of ORF7a generally increased. Notably, this approach failed to detect expression of leaders immediately adjoining ORF7b or ORF10 (Table S3 (Taiaroa et al., 2020)).

By visual inspection, Caco-2 cells appear hardly affected by the infection; whereas, Calu-3 clearly show signs of impaired growth and cell death at 24 hr post infection (hpi), particularly when infected with SARS-CoV-2 (Figure S1I). Data from that time point, including e.g. the level of viral RNA (Figure 1A) should be therefore interpreted with caution. Taken together, we show that the three infected cell lines show distinct responses in respect to the course of SARS-CoV/-2 infection.

SARS-CoV-2 infection leads to a two-fold stronger induction of ISGs compared to SARS-CoV

To analyze changes in the host cell transcriptome, we compared virus- and cell line-dependent differences in gene expression. SARS-CoV-2 infection of Calu-3 cells, as expected from similar results for SARS-CoV infections (Yoshikawa et al., 2010), led to induction of a range of genes known to respond to viral infections,

such as IFIT2, OAS2, or IFNB1 (Figure 2A) (Schoggins, 2019). This likely occurs through triggering of RNA sensors by incoming viral RNA via IRFs and NF-κB signaling (Schneider et al., 2014; Schoggins, 2019). Expression levels of these genes at 12 hpi were on average about twice as high in cells infected with SARS-CoV-2 compared to infection with SARS-CoV (Figure 2B), at similar amounts of viral RNAs present in the cells at 12 hpi (Figure 1A, right panel). This difference in the extent of the transcriptional response in SARS-CoV/-2 infections has also been observed in human airway epithelial cells (AECs) (V'kovski et al., 2020). Importantly, several cytokines (Carrasco Pro et al., 2018) are among the induced genes (Figure 2C), and which might be connected with pathologies such as the acute respiratory distress syndrome (ARDS) in CoV infections (Channappanavar and Perlman, 2017; Moore and June, 2020).

Expression of arrestin-related domain-containing protein-3 and thioredoxin-interacting protein genes is induced independently of RNA sensing

Although the infection levels are comparable between Caco-2 and Calu-3 cells, based on the amount of intracellular viral RNA and virion yield (see above), the host transcriptome responses were markedly different (Figures 2D and S2A). Both cell lines showed an increase in expression of a number of genes typically activated in response to ER stress and MAP kinase activation (e.g. activating transcription factor 3, early growth response 1, EGR1; immediate-early response 3; protein phosphatase 1 regulatory subunit 15A (PPP1R15A) also known as growth arrest and DNA-damage-inducible 34; GADD34 (Lee et al., 2018)), with a corresponding enrichment of related GO terms in a gene set enrichment analysis (Figures 2E and S2B). Induction of genes regulated by IRFs was however absent in the Caco-2 cells employed here. One reason for this response might be the low expression of the pattern-recognition receptors IFIH1 and DDX58 (Figure S2C).

In addition, two genes, arrestin-related domain-containing protein-3 (ARRDC3) and thioredoxin-interacting protein (TXNIP), stood out among the few genes that were significantly upregulated upon infection with either viruses and in both cell lines (Figures 2D and S2A). Both genes encode proteins that are involved in regulation of signaling pathways (Aubry et al., 2009). ARRDC3 mediates G protein–coupled receptor lysosomal sorting and apoptosis-linked gene 2-interacting protein X (ALIX) ubiquitination (Dores et al., 2015). ALIX is a Lys63-specific polyubiquitin binding protein that functions in retrovirus budding and Dengue virus propagation (Dowlatshahi et al., 2012; Thepparit et al., 2019). TXNIP is involved in the regulation of glucose and lipid metabolism (Alhawiti et al., 2017) and has been shown to be involved in initiation and perpetuation of NLRP3 (nucleotide-binding domain and leucine-rich repeat and pyrin domain containing 3) inflammasome activation (Elliott and Sutterwala, 2015; Oslowski et al., 2012).

To conclude, most gene expression changes in response to SARS-CoV-2 infection are likely triggered by RNA sensors and/or ER stress. In H1299 cells, in which virus replication was very inefficient, we observed no consistent and notable differences in gene expression, as well as no alterations of the visual appearance (data not shown).

Comparison of datat sets from *in vivo* and *in vitro* infections shows common and distinct responses to SARS-CoV-2 infections

To substantiate the relevance of the genes induced by the SARS-CoV-2 infection observed in the Calu-3 cells, we compared our data with various recently published data sets. This includes bronchoalveolar lavages (BALs) (Liao et al., 2020), as well as nasopharyngeal swabs (Chua et al., 2020) of patients infected with COVID-19 , and transcriptome studies of normal human bronchial epithelial (NHBE) cells, A549 cells with and without ACE2 expression, and also Calu-3 cells upon infection with SARS-CoV-2 (Blanco-Melo et al., 2020). (Table S2). For the BAL samples, differential gene expression was calculated for the epithelial cells (Figure S2D upper panel), from severe COVID-19 cases in comparison to the healthy control also used in the original paper (Figure 2F). Several genes were also found to be induced in the patient samples, such as several IFI/IFIT/IFITM genes, as well as the cytokines C-C motif chemokine ligand 5 (CCL2) and C-X-C motif chemokine ligand 9 (CXCL10), which were also upregulated in a BAL bulk RNA-seq analysis (Xiong et al., 2020). Remarkably, we did not observe induction of interferon genes, pro-inflammatory cytokines, and IL-6 in epithelial cells in patient samples. ARRDC3 and TXNIP, the two genes upregulated in both Calu-3 and Caco-2 cells, generally showed low expression with no induction in this analysis. However, when comparing expression levels within samples, we found an increase of ARRDC3 expression in a subset of patients compared to the healthy control, along with the consistent upregulation of the stress gene PPP1R15A (Figure S2D lower panel).

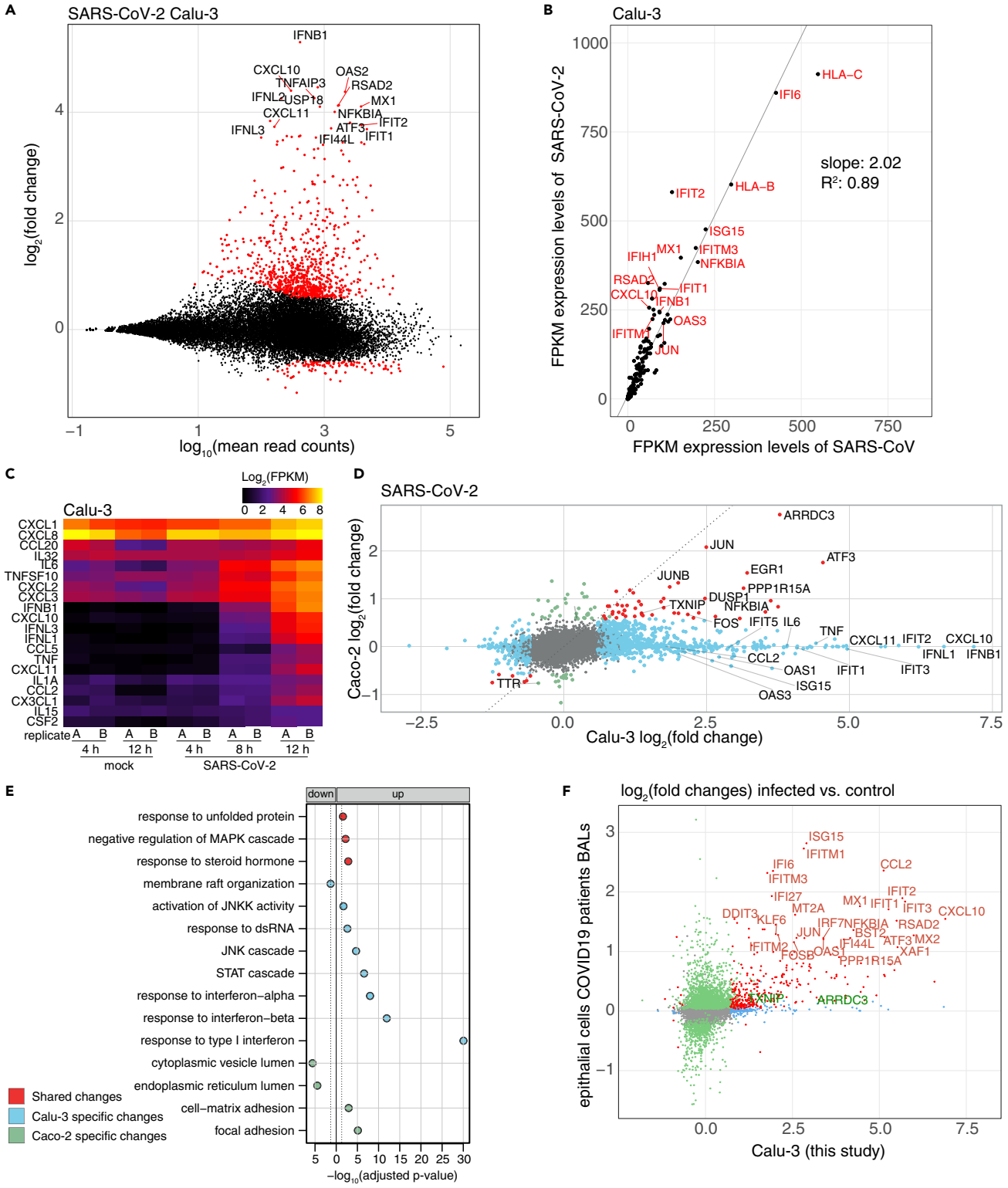

Figure 2. Dissection of the transcriptional response to SARS-CoV/-2 infection

(A) Mean average vs. $\log_2$ fold change plot of differentially expressed (DE) genes at the mRNA level of Calu-3 cells infected with SARS-CoV-2 (12 hpi). X axis depicts $\log_{10}$ of mean counts associated with a gene. Y axis depicts mRNA $\log_2$ fold changes. Significant differentially expressed genes (red dots) are defined as those with an absolute $\log_2$ fold change of greater than 0.58 and a Benjamini-Hochberg corrected adjusted p value > 0.05. Selected outliers are labeled.

Figure 2. *Continued*

(B) Expression values (FPKM) of genes significantly induced in cells infected with either virus at 12 hpi in Calu-3 cells. Values represent averages of the two replicates.

(C) Expression values (FPKM) of differentially expressed cytokine genes in SARS-CoV-2 infected Calu-3 cells. Values of individual replicates are $\log_2$ transformed and represented as a heatmap.

(D) $\log_2$-transformed fold changes of SARS-CoV-2 infected Calu-3 cells at 12 hpi vs. mock (horizontal axis) and Caco-2 cells 12 hpi vs. mock (vertical axis). Genes exhibiting significant changes in both cell lines are shown in red, significant changes only in Calu-3 cells in light blue, only in Caco-2 cells in light green. All other genes are shown in gray. Selected genes with significant fold changes are labeled.

(E) Gene Ontology (GO) terms in a gene set enrichment analysis of cell lines infected by SARS-CoV-2. In blue are indicated enriched GO terms from differentially expressed genes in Calu-3 cells, in green from Caco-2 cells and in red from both cell lines. Adjusted p values were -$\log_{10}$-transformed. GO terms from downregulated genes are shown to the left, those from upregulated genes on the right of the solid line. The dotted line represents the cutoff value ($p = 0.1$).

(F) Log_2-transformed fold changes of SARS-CoV-2 infected Calu-3 cells of this study at 12 hpi (horizontal axis) and epithelial cells from severe COVID19 patients from Liao et al. (2020) (vertical axis). Genes exhibiting significant changes in both cells are shown in red, significant changes only in Calu-3 cells in light blue, only in patient cells in light green. All other genes are shown in gray. Selected genes with significant fold changes are labeled in red, and additional genes mentioned in the text (TXNIP and ARRDC3) in green.

Within the epithelial cells in nasopharyngeal swabs, the highest expression values for the SARS-CoV-2 receptor ACE2 was found in secretory and ciliated cells (Chua et al., 2020), and we performed a similar analysis as above for these two cell types by comparing differential expression between the five control samples and the nineteen samples from infected patients (Figure S2E). The differentially expressed genes, which were commonly upregulated in patient samples, showed a smaller overlap with the Calu-3 cells compared to the BAL samples.

Infection of Calu-3 cells with SARS-CoV-2 showed strong reproducibility across experiments from our study (Figure S2F) and data from other laboratories (Figure S2G, upper panel). There were however considerable differences between Calu-3 and NHBE cells on one side (Figure S2G, lower panel), and A549 cells (Figure S2H) on the other side. As in the patient samples, interferon beta/lambda genes were not induced in NHBE cells (Figures 2F and S2G). On the other side, CXCL10 or IFIT2, which were induced in patient samples and Calu-3 cells, were not or not reproducibly induced in NHBE (Figure S2G) or A549 cells (Figure S2H). This however could also be due to variabilities in e.g. employed MOIs (Blanco-Melo et al., 2020). Taken together, the interferon and stress response observed in SARS-CoV-2 infected Calu-3 cells could be partially recapitulated in patient samples and other cell lines. Further investigations are warranted to better define appropriate model systems for studying the consequences of *in vivo* SARS-CoV-2 infections.

MicroRNA miR-155-3p is expressed in SARS-CoV and SARS-CoV-2 infected cells

In addition to assessing mRNA changes, we have also profiled small RNAs expression changes in the context of Calu-3 infections. Both viruses triggered a close to 16-fold upregulation of miR-155-3p, the "star" form, and an almost 3-fold upregulation of miR-155-5p (Figures 3A, 3B, and S3A). Importantly, the primary miRNA precursor gene, miR-155 host gene (MIR155HG), was also upregulated in polyA-seq and total RNA-seq data by about 10-fold, suggesting that the increase of two miRNAs was primarily driven by transcription (Figure S3B). In addition, we found a significant upregulation of miR-4485. All observations were confirmed using a Taqman assay (Figure 3C). Of note, miR-4485 derives from the MTRNR2L8 locus, and it is unclear whether its expression pattern reflects its functionality or that of its host gene.

Interestingly, the miRNA profiling identified small RNAs mapping to vault RNA (VTRNA) genes to be induced by the infection (Figures 3D and S3C–S3E). The predominant lengths of these RNAs were 21 and 24 nt (Figure S3C). The function of vtRNAs has not been fully elucidated, but the mature VTRNA1-1 was recently discovered as a negative regulator of autophagy (Horos et al., 2019). VTRNA-derived sRNAs can be processed by DICER and bound by Argonaute proteins (Persson et al., 2009; Thomson et al., 2015) and could thus have a regulatory role in virus infected cells.

scRNA-seq of infected Calu-3 cells shows expression of interferon genes only in a small subset of cells

To assess gene expression changes on the level of individual infected Calu-3 cells, we performed scRNA-seq at different time points post infection for both SARS viruses. The data showed that cellular transcriptomes grouped by time point of infection (Figure 4A) and type of virus (Figure 4B). At 4 hpi, the number of cells bearing viral RNA was between 40% and 60% (Figure S4A, Table S4). At 8 hpi and 12 hpi, all cells contained viral RNA. The distribution of viral load (percentage of viral RNA per cell) was comparable for the two

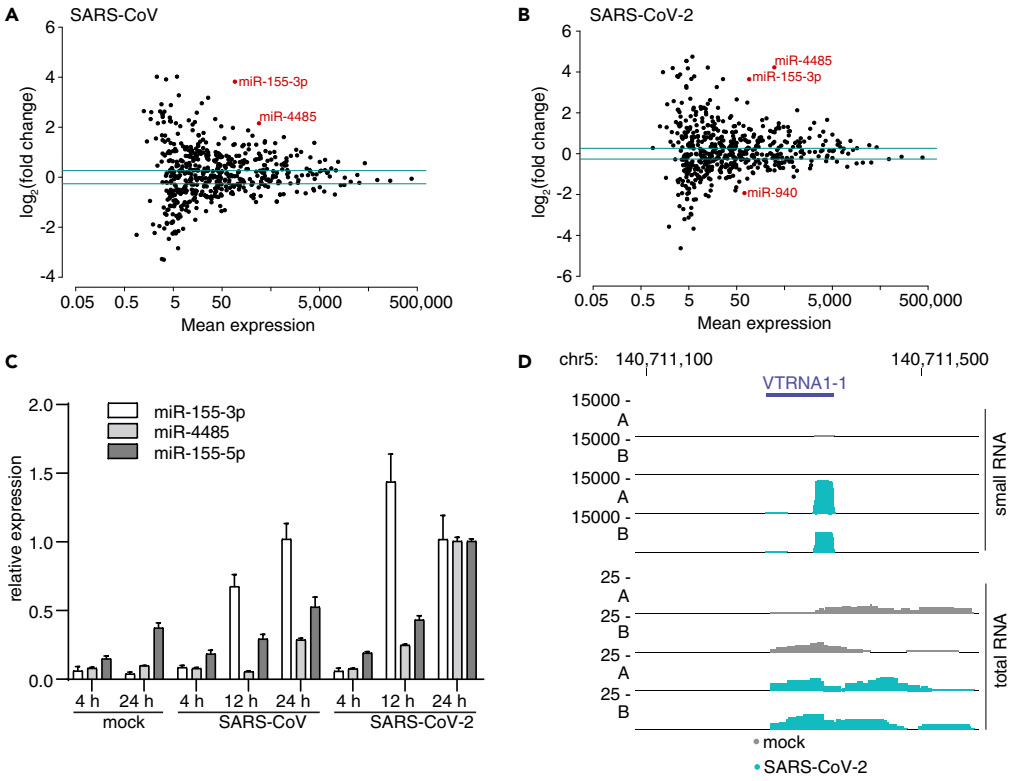

Figure 3. MicroRNA miR-155 and vaultRNA-derived miRNAs are induced by the infection

(A and B) Scatterplots of miRNAs from of SARS-CoV (A) or SARS-CoV-2 (B) infected Calu-3 cells harvested at 12 hpi. Plotted are mean expression over log2(fold changes), normalized to mock infected (uninfected) cells. miRNAs found significantly differentially expressed are indicated in red.

(C) Validation of the induction of the displayed microRNAs in Calu-3 cells at 12hpi using Taqman assays. Shown are average and standard deviations of three measurements from one biological replicates of the samples used for the sequencing in A and B, as relative expression normalized to 24 hpi SARS-CoV-2.

(D) Coverage plots of the vaultRNA gene VTRNA1-1 of replicates A and B at 12hpi after infection of Calu-3 cells with or without SARS-CoV-2.

viruses and showed the expected increase from 4 hpi to the later time points after infection; however biological replicates showed some variability (Figures S4B and S4C). The amount of detected RNA molecules (UMI, unique molecular identifiers) was generally lower in cells with high levels of viral RNA (Figure S4D), indicative of some degree of host cell shutoff.

In agreement with the bulk RNA-seq data, we observed a strong increase of e.g. IFIT2 or OAS2 in infected cells (Figures 4C and S4E). Again, the induction of these genes was much stronger in the cells infected with SARS-CoV-2 compared to infection with SARS-CoV (Figures 4C and S4E).

In the bulk RNA-sequencing data, interferon beta (IFNB1; Figure 2A) was one of the most induced genes upon SARS-CoV-2 infection. In the scRNA-seq data, we found the expression of IFNB1 expression restricted to a small subset of infected cells (Figure 4D). As in bulk RNA-sequencing, we observed expression of ARRDC3 in cells infected with either viruses. ARRDC3 (Figure 4E), as well as PPP1R15A (Figure S4F), were highly expressed in cells with the highest levels of viral RNA. For SARS-CoV infection, we observed similar effects, however at overall lower levels and in very small numbers of cells (Figure 4D, top part of the plots).

To confirm the induction of the microRNA mir-155 described in the previous section, we investigated the expression of its host gene, MIR155HG. Although it is expressed at only low levels, it resembled the expression pattern of IFIT2 and OAS2 genes (compare Figure S4G with Figure S4E), i.e. induction in cells containing SARS-CoV-2 RNA and high levels of SARS-CoV RNA.

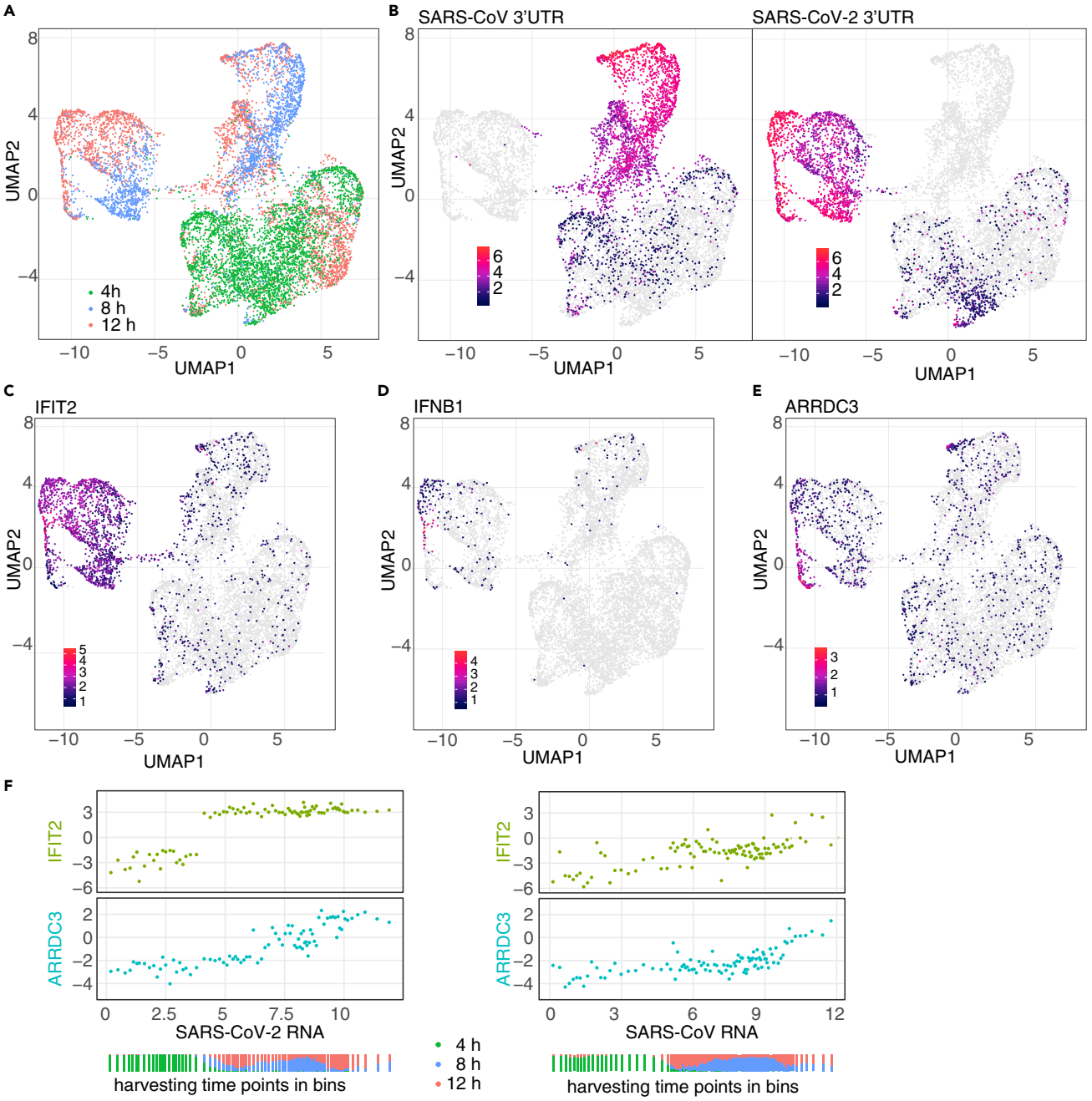

Figure 4. Single-cell RNA-sequencing shows different expression dynamics of genes induced by infection

(A) Based on scRNA-seq data, Calu-3 cells were embedded into diffusion map space and, by Uniform Manifold Approximation and Projection (UMAP), projected using 20 diffusion components into two-dimensional space, and colored by harvesting time point.

(B) Same projection as in A, with cells colored by SARS-CoV (left) and SARS-CoV-2 (right) 3′-UTR signal.

(C–E) Same projection as in A, with cells colored by expression levels of IFIT2 (C), IFNB1 (D), and ARRDC3 mRNA (E).

(F) Cells were sorted by the amount of viral RNA and binned. Horizontal axis for each panel represents relative, $\log_2$-transformed levels of SARS-CoV-2 RNA (left) or SARS-CoV (right) RNA per bin. The vertical axes in the panels represent relative, $\log_2$ transformed expression levels for IFIT2 (upper panel) or ARRDC3 (lower panel). Every dot represents a bin containing 50 cells. The distribution of the harvesting time points of the cells per bin is indicated below.

To relate host gene expression to the accumulation of viral RNAs, cells were ordered by an increasing amount of viral RNA and arranged into bins of 50 cells. This was done to reduce noise due to detection dropout events. The correlation with viral RNA over all bins was then calculated for both viruses, indicating a particularly strong

relationship for the amount of viral RNA the expression of, among others, ARRDC3 (Figure S4K). For IFIT2 and ARRDC3, the expression level per bin was then plotted against the amount of viral RNA (Figure 4F, left). For IFIT2, a stepwise expression increase between 4 hpi and 8 hpi was observed, with the expression levels afterward being independent of the amount of SARS-CoV-2 RNA. ARRDC3 mRNA transcript levels however increased gradually with the accumulation of viral RNA. For SARS-CoV, this transcriptional induction was observed only at much higher levels of viral RNA were (Figure 4F, right).

In order to identify genes co-regulated with IFNB1, we performed a correlation analysis of cells binned by increasing IFNB1 and ARRDC3 expression (Figure S4L). Using this approach, we found a putative co-regulation of the four interferon lambda genes (IFNL1-4), the chemokine genes, CXCL9 and CCL5, and the cholesterol-25-hydroxylase gene. This enzyme, as well as its product 25-hydroxycholesterol, has been shown to act against a range of viruses (Liu et al., 2013). In addition, two other genes were found in this group, the sodium voltage-gated channel alpha subunit 3 gene (SCN3A) (Figure S4M) and the dual oxidase 1 gene (DUOX1) (Figure S4N). Although SCN3A has previously not been described in the context of virus infections, DUOX1 appears to promote the innate immune defense to pathogens via the production of reactive oxygen species (De Deken et al., 2014).

RNA velocity reveals transient induction of interferon genes and temporal resolution of NF-κB signaling

To better understand the nature of interferon beta/lambda gene induction in the context of SARS-CoV-2 infection, we applied RNA velocity, which uses sequencing reads originating from introns to measure the amount of nascent mRNA (La Manno et al., 2018). This analysis inferred a temporal trajectory, represented by the black arrows in Figure 5A, with longer arrows indicating a stronger signal. For the SARS-CoV-2 infected cells, the directionality was particularly strong from cells expressing interferon and interferon-correlated genes to the cells with maximal amount of viral RNA but not expressing interferon genes (Figure 5A). This finding suggests that induction of interferon genes is short and transient during the viral replication. A similar effect was seen for SARS-CoV infection. We observed that target genes of IRFs such as IFIT2, IFIT1, or OAS2 (Grandvaux et al., 2002) show high intron counts in most of the cells infected with SARS-CoV-2, except for a subpopulation (Figure 5B underneath the blue oval, S5B). This subpopulation, however, showed intron counts for NF-κB target genes such as interleukin 6 (IL6), tumor necrosis factor (TNF) or NF-κB inhibitor alpha (NFKBIA) (Figure 5C bottom part of the violet oval, S5B). Since the IFNB1 gene is devoid of introns and intron counts from IFNL1-4 were not detected, we used CCL5 as a reference for this group of genes (compare Figure S5A with Figure 4D, middle panel). Interestingly, we found that its transcriptional activity is restricted to a small subset of cells (Figure 5D) at the intersection of IRF and NF-κB activity.

To identify the temporal evolution of changes in gene expression, we have looked at the patterns of host and viral gene expression in the principled space of a diffusion map (Angerer et al., 2016; Haghverdi et al., 2016). As expected, the cells infected with the two viruses separated on two branches according to the main diffusion components (Figure S5C). Especially for SARS-CoV-2, there was a noticeable population of cells (Figure S5C, circled by a violet oval) marked by high levels of both viral RNA and IL6 mRNA, whereas the highest levels of IFNB1 and IFIT2 mRNA were in distinct subpopulations, indicating the importance of higher order diffusion components for the proper temporal stratification (Figure S5C, pink and blue ovals). To corroborate the velocity analysis shown in Figure 5A, we projected the velocity data on an alternative embedding, initialized with diffusion pseudotime, i.e. reflecting cell-to-cell transition probabilities (Figure S5D). In there, we observed the same biological effect as in Figure 5, namely that transient induction of interferon genes is followed by expression of NF-κB target genes.

For a comprehensive analysis, we have binned SARS-CoV-2 infected cells by applying the Louvain algorithm on the top fifty diffusion components and sorted the resulting bins by median SARS-CoV-2 load (Figure 5E, top row). Per bin, the intron counts of the infection-induced genes IFIT2, OAS2, CCL5, IL6, NFKBIA, and TNF are shown, along with ATXN10 as control (Figure 5E). The temporal ordering suggests that IRF-regulated genes (OAS2, IFIT2) were transcribed before NF-κB target genes (IL6, NFKBIA, TNF), and likely only during a relatively short time window, both pathways were active and drove transcription of interferon and related genes (CCL5).

In addition, we performed the RNA velocity analysis on an embedding of the Calu-3 cells calculated without viral genes, which is now driven by the genes induced by the infection such as IFIT2 or ARRDC3, leading to a convergence of highly infected cells independent of the virus (Figure S5E).

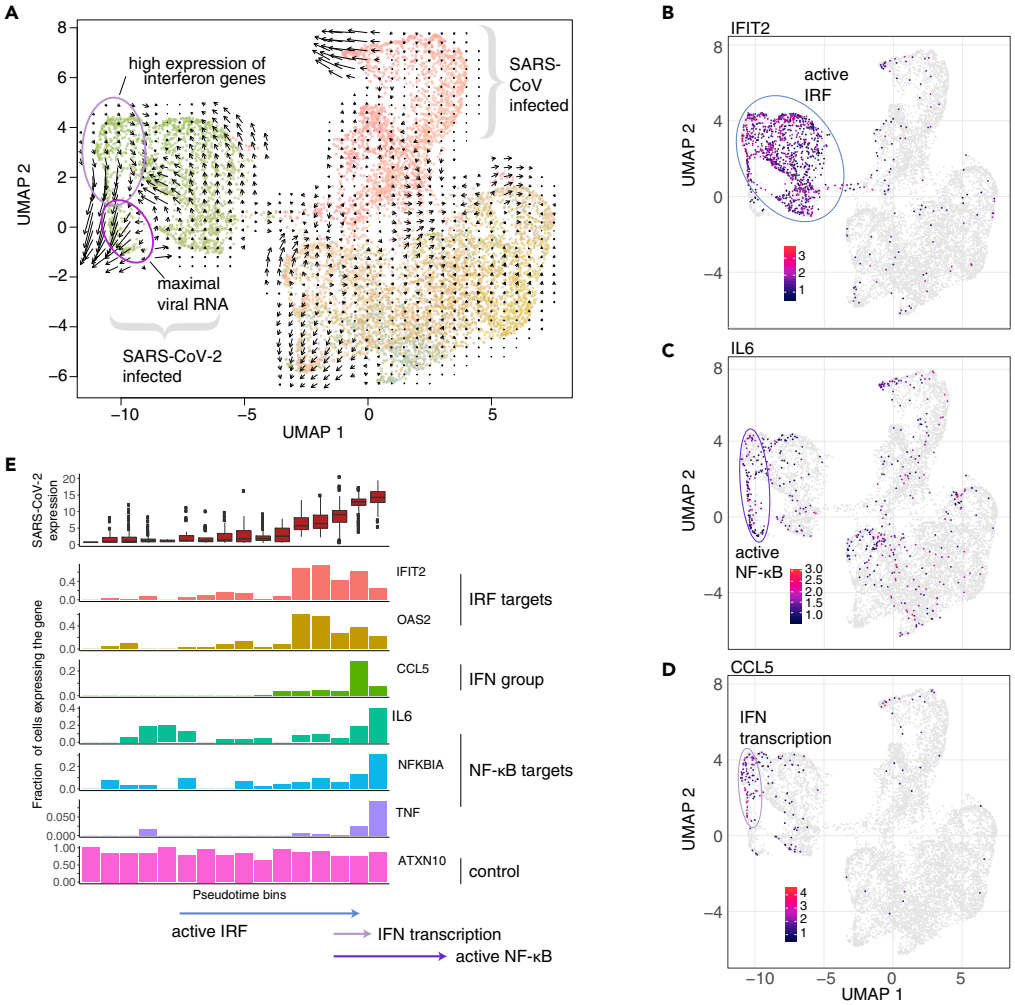

Figure 5. Interferon genes and NF-κB target genes are expressed in small subsets of cells

(A) Embedding as in Figure 4. Areas of interest are marked by colored ovals and labeled. Arrows represent trajectories based on RNA velocity, signal strength is represented by the length of the arrows.

(B–D) Projection as in A, but colored by intron counts of IFIT2 (B), IL6 (C), and CCL5 (D). Areas of interest are marked by colored ovals and labeled.

(E) Cells were grouped into pseudotime bins. Plotted are, from top to bottom, the amount of SARS-CoV-2 viral RNA, and the percentage of cells with intron counts for the indicated genes.

Interestingly, we also observed a minor increase in intronic counts for ACE2 transcripts in SARS-CoV-2 infected cells (Figures S5F and S5G), suggesting a transcriptional activation of the viral receptor gene during infection, as observed recently (Ziegler et al., 2020).

scRNA-seq of SARS-CoV and SARS-CoV-2 infected H1299 reveals a potential involvement of HSP90AA1 in the progression of infection

As shown above, transcriptional changes in bulk and scRNA-seq data from Calu-3 infected cells were dominated by the interferon response. In order to detect more subtle alterations in the cellular transcriptomes, we applied the scRNA-seq likewise to SARS-CoV/-2 infected H1299 cells, which are only partially permissive to the infection.

Despite the overall low amount of viral RNA in infected H1299 cells (Figure 1A), the percentage of cells bearing viral transcripts was unexpectedly high (Figure S6A, Table S4), indicating that virions indeed are able to enter the cells. As seen in the bulk RNA-seq, transcriptional changes were subtle, and cells do

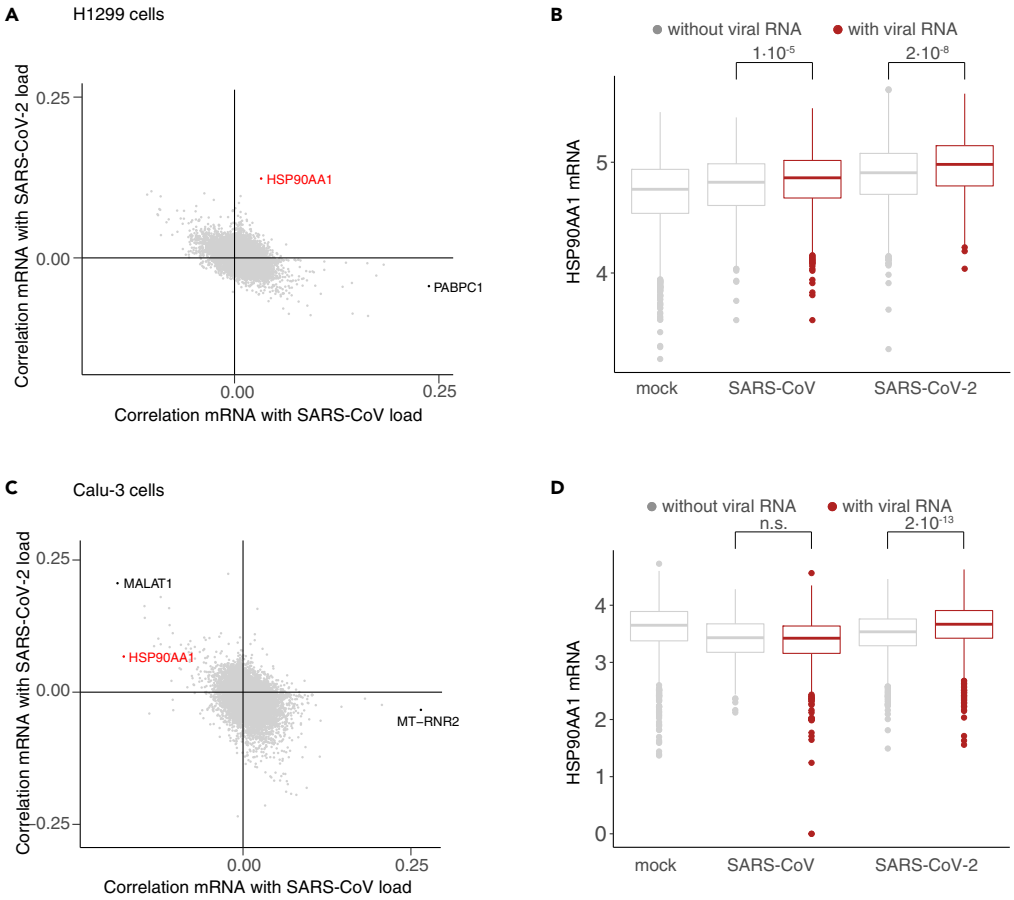

Figure 6. HSP90AA1 is deregulated in SARS-CoV-2 infected cells

(A) Correlation of gene expression values with the amount of SARS-CoV RNA (horizontal axis) and SARS-CoV-2 RNA (vertical axis) in the H1299 scRNA-seq data.

(B) Distribution of HSP90AA1 mRNA expression in H1299 single cell samples. For SARS-CoV and SARS-CoV-2 samples, cells were group by presence of viral RNAs. To calculate p values, the Kruskal-Wallis test was used (p.val < 1×10^{-5}, with 3 degrees of freedom), followed by post-hoc comparison of classes using the Dunn test with Bonferroni correction. Non-significant (n.s.) indicates p values larger than 1×10^{-5}.

(C and D) As in A, B, but for Calu-3 (4 hpi) samples.

not group into discrete clusters (Figures S6B–S6D). When correlating individual genes with the amount of viral RNA over cells, we found a positive correlation with HSP90 alpha family class A member 1 (HSP90AA1) with the amount of SARS-CoV-2 RNA but not SARS-CoV (Figure 6A). When comparing expression within samples, we observed higher levels of HSP90AA1 mRNA in cells with SARS-CoV-2 viral RNA compared to those without (Figure 6B). To exclude that this would not be a general effect for highly expressed transcripts, we performed the same analysis for GAPDH, which remained unchanged in virus-positive cells (Figure S6E).

For the Calu-3 cells, we found a similar HSP90AA1 expression pattern in the data from the 4 hpi time point (Figures 6C and 6D). However, in this analysis, we observed, like for HSP90AA1, a positive correlation of MALAT1 RNA levels with the amount of viral RNAs in the cells (Figures 6C and S6F). Previously, MALAT1 was shown to be upregulated by the UPR during flavivirus infection (Bhattacharyya and Vrati, 2015).

In order to investigate HSP90AA1 mRNA deregulation in patients infected with COVID-19, we re-examined the BAL scRNA-seq (Figure 2F). We observed that in a cluster of epithelial cells, with a substantial number of cells containing viral RNA, HSP90AA1 was among few genes that were deregulated in cells with viral transcripts compared to those without (Figure S6G).

Overall, we found HSP90AA1 deregulation in various datasets, suggesting a role for HSP90AA1 in SARS-CoV-2 infection.

Inhibition of HSP90 reduces viral yield and expression of cytokine genes

The involvement of HSP90AA1, a highly-conserved molecular chaperone, in viral infections has since a long time been discussed to be involved in the infection of a range of viruses (Geller et al., 2012). In order to explore the effect of HSP90 on SARS-CoV-2 replication in Calu-3 cells, we applied the HSP90 inhibitors Onalespib, Ganetespib, and 17-(Allylamino)-17-demethoxygeldanamycin (17-AAG) to cells one hour after viral absorption and measured virus yield and RNA in the supernatant at 16 hpi. At inhibitor concentrations of 800 nM, viral yield was reduced by about 50%–70% (Figure 7A). Cell viability was not impaired using the indicated inhibitor concentrations (Figure S7A). In order to assess the production of intracellular viral RNA and changes in host gene expression, we performed bulk RNA-sequencing of uninfected cells, as well as DMSO (solvent control) and HSP90 inhibitor treated infected cells. Intracellular viral RNA was reduced comparable to viral yield (Figure 7B). The treatment of cells with HSP90 inhibitors dampened the upregulation particularly of pro-inflammatory cytokines, including IL-6, CXCL10, and CXCL11 (Figures 7C and S7B). In summary, inhibition of HSP90 reduced both the viral replication and the induction of the inflammation response.

To assess the effect of HSP90 inhibition in primary human cells, we used AEC differentiated *in vitro* from human lung tissue obtained from pneumonectomy specimens (Imai-Matsushima et al., 2018). Again, SARS-CoV-2 replication was considerably slower upon treatment with the HSP90 inhibitor 17-AAG at 200 nM (Figure 7D). Under these conditions, cell viability was not impaired (Figure S7C). We again assessed changes in host gene expression by RNA-sequencing, and observed a reduction of mRNA levels of various genes induced by the infection, including the cytokines CXCL10 and CXCL11 (Figure 7E). As observed in Calu-3 cells, chemical inhibition of HSP90 in infected human primary cells reduced viral replication and the induction of the inflammatory response, suggesting that 17-AAG or other HSP90 inhibitors already applied in clinical trials could be used for the therapeutic interventions in the treatment of COVID-19.

DISCUSSION

We performed gene expression profiling of three different human cell lines infected with SARS-CoV and SARS-CoV-2 at bulk and single-cell level. We show a particularly strong induction of a range of genes commonly induced by virus infections in Calu-3 cells, including cytokines, by SARS-CoV-2 in both bulk and scRNA-seq experiments. For various CoVs, a range of mechanisms that interfere with interferon signaling have been reported (Kindler et al., 2016). For SARS-CoV, it was shown that ORF6 inhibits signal transducer and activator of transcription (STAT) signaling (Frieman et al., 2007) and that IRF3 activity is impaired (Spiegel et al., 2005). Since RNA levels per cell (Figure S4A) and on the population level were comparable (Figure 1A), it is tempting to speculate that such mechanisms could be less efficient in SARS-CoV-2 compared to SARS-CoV.

By comparing the transcriptional response of Calu-3 cells to that of Caco-2 cells, which might have reduced capability to sense incoming RNA (Figure S1A), we identify genes induced independently of the RNA sensing system, such as the ER stress marker PPP1R15A. We also observed upregulation of the genes TXNIP and ARRDC3. Both are involved in signaling processes, and further investigations into their role in SARS-CoV-2 infection are warranted.

On the other hand, in H1299 cells, viral replication was very inefficient both in terms of extracellular viral yield and intracellular viral RNA. The percentage of cells with viral reads in the single-cell experiment (Figure S6A) is relatively high, but in contrast to the Calu-3 cells not consistently increasing over time. Whether this means that virus particles do not productively enter into the cytoplasm, or suppression of replication in these cells, cannot be answered from our data.

Small RNA profiling indicated an increased expression of miR-155 in the infected cells. This miRNA has been associated with various virus infections (Badry et al., 2020; Dickey et al., 2017; Gottwein, 2013; Zeng et al., 2015). miR-155-3p is also a well-known regulator of immune cells, in particular T cell differentiation (Mehta and Baltimore, 2016; Thai et al., 2007). Involvement of this miRNA in the regulation of innate immunity has also been reported (Zhou et al., 2010). Recently, miR-155-5p expression was shown to be induced in mice infected with influenza A virus (Woods et al., 2020). Importantly, in this study, lung injury

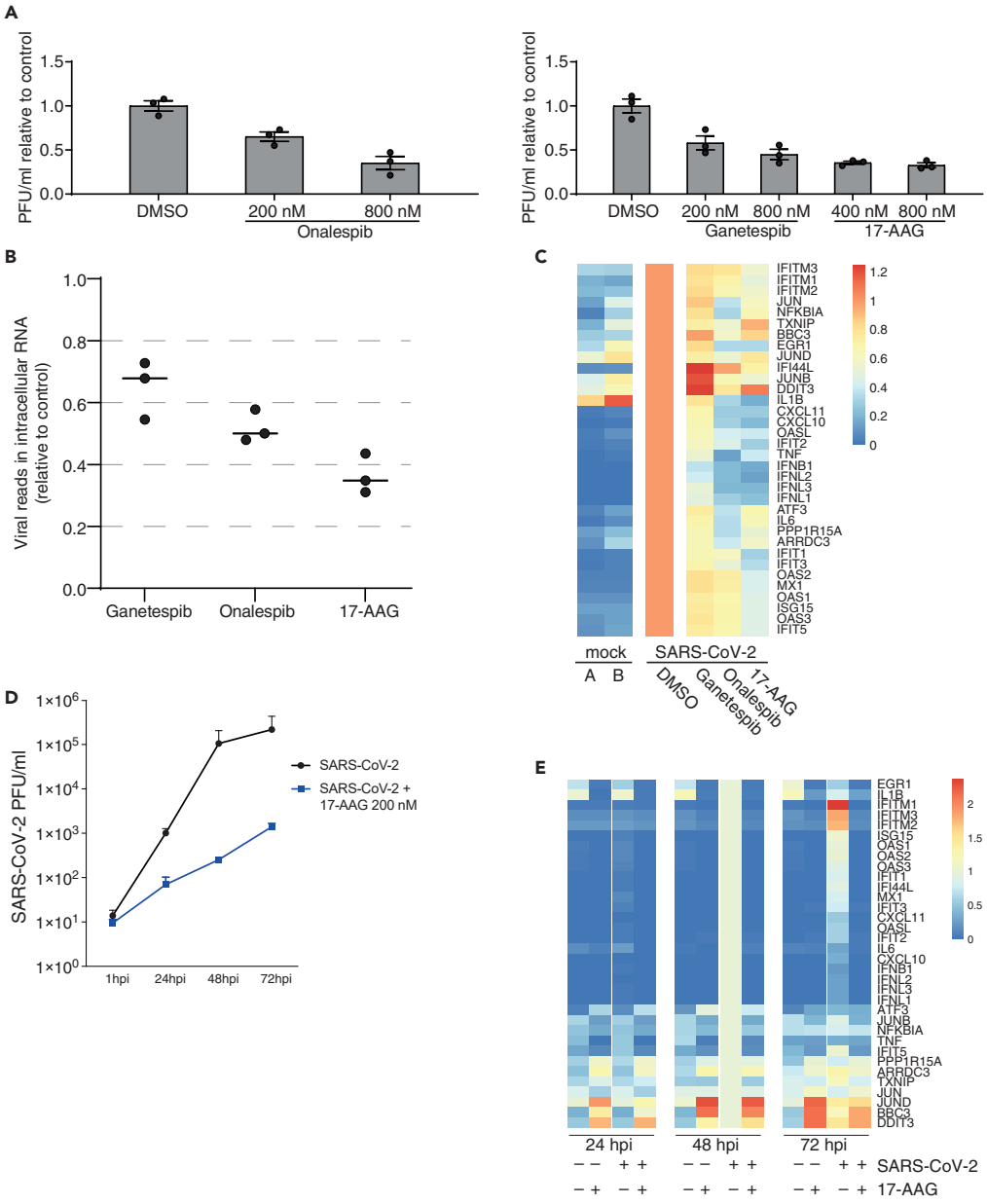

Figure 7. HSP90 inhibitors treatment reduce SARS-CoV-2 replication and induction of pro-inflammatory cytokines

(A) Fold change of infectious plaque-forming units (PFUs) in supernatants of Calu-3 cells infected with SARS-CoV-2 with the indicated treatment 16 hpi. After viral adsorption for one hour, cells were washed and supplied with conditioned medium containing DMSO, as solvent control, or indicated concentrations of Onalespib, Ganetespib, or 17-AAG. Experiment performed in triplicates, and error bars represent standard deviations.

(B) Percentage of viral sequencing reads of all reads in Calu-3 cells after 800 nM of indicated inhibitor treatment 16 hpi.

(C) Heatmap of selected induced genes normalized to infection in Calu-3 cells without treatment.

(D) Infectious viral particles in the supernatant at the indicated timepoints post infections of primary human airway epithelial cells (AECs) treated with either DMSO (control, black) or 200 nM 17-AAG (blue).

(E) Heatmap of selected induced genes in AECs normalized to the infection sample treated with DMSO of the same timepoints (average of normalized expression values/FPKM).

by ARDS was attenuated by deletion of miR-155, making this miRNA a potential therapeutic target in the context of COVID-19.

The scRNA-seq experiments provided a rich dataset to analyze host cell expression changes in response to the infection. Surprisingly, the percentage of cells containing viral RNA was much higher than expected based on the MOI used for the infection experiments. A possible explanation for this observation could be viral spreading by cell-to-cell fusions, facilitated by the S protein on the cell surface (Buchrieser et al., 2020; Masters, 2006). Furthermore, the analysis of the scRNA-seq data of infected Calu-3 cells indicated a sequential activation of IRF and NF-κB target genes, and in particular, a putatively strong, but transient, induction of interferon genes. This could be due to a relatively short time window during the progression of infection, in which both IRF and NF-kB are sufficiently activated to trigger interferon gene transcription (Czerkies et al., 2018; Iwanaszko and Kimmel, 2015).

Concomitantly with the interferon induction, we observed a small increase in transcription of ACE2 mRNA in cells infected with SARS-CoV-2. Changes in ACE2 transcript levels in the context of interferon treatment and CoV infection have been described before (Gralinski and Baric, 2015; Ziegler et al., 2020). However, further studies are needed to explore whether mRNA changes are reflected on the protein level, particularly since a recent report indicates that the transcriptionally upregulated ACE2 mRNA does not yield functional protein (Onabajo et al., 2020). Although the transcriptional induction (RNA velocity) was detectable, changes in mature mRNA levels were moderate in comparison to IRF-driven genes such as the IFIT family.

Cell line and cell culture-based infections allow detailed analyses of molecular changes during infections, since perturbations such as genetic manipulations or compound treatments can be straightforwardly applied. However, they come with limitations and focus on isolated cells apart from tissues or organisms. This involves e.g. the production of cytokines, which was described to be connected to COVID-19 pathogenesis (Blanco-Melo et al., 2020; Channappanavar and Perlman, 2017; Moore and June, 2020). Here, infected Calu-3 cells showed a strong increase in expression of a number of chemokines, interferons, and pro-inflammatory cytokines, whereas A549 and NHBE cells responded with an induction of pro-inflammatory cytokines (Figure S2). However, in epithelial cells from BALs of patients infected with COVID-19, IL-6 or TNF mRNAs were barely detectable. Since these and interferon genes were transcriptionally activated only in small subsets of Calu-3 cells, this could represent an unlikely physiological cellular state. Overall, how to best match processes happening in the human body using *in vitro* models will require further investigations using a range of models and detailed matching with patient data (Butler et al., 2018; Duan et al., 2020; Lamers et al., 2020; Stanifer et al., 2020).

CoVs induce ER stress and activate the UPR in infected cells (Fung et al., 2016; Versteeg et al., 2007). We observed transient deregulation of the stress-responsive HSP gene HSP90AA1 (Zuehlke et al., 2015), in both the "slow-motion" infection model, H1299 cells, and in Calu-3 cells (4 hpi), and in subsets of epithelial cells in patient samples. HSP90 modulates UPR by stabilizing the ER stress sensor transmembrane kinases IRE1α (Marcu et al., 2002). Inhibition of the HSP90 has previously been shown to slow down the replication of several viruses (Gao et al., 2014; Geller et al., 2012; Katoh et al., 2017; Li et al., 2004). The reduction of SARS-CoV-2 growth by HSP90 inhibition was also proposed based on a computational analysis of patient RNA sequencing data (Sultan et al., 2020). Here, we show that inhibition of HSP90 by three different compounds at high nanomolar concentrations can reduce virus replication in an *in vitro* infection model. Interestingly, IFIT2 mRNA levels seemed unaffected by HSP90 inhibition, supporting the "on-off-switch" independent of the amount of viral RNA observed in the scRNA-seq data. In addition, mRNA expression of the pro-inflammatory cytokines TNF and IL1B, which are implied in the progression of COVID-19 (Hirano and Murakami, 2020), were strongly reduced. This repression is likely due to the requirement of HSP90 for constitutive and inducible IKK and NF-κB activation (Broemer et al., 2004). Interestingly, in addition to the already described activities, HSP90 inhibitors were shown to exert barrier protective effects on pulmonary arterial endothelial cells and were suggested to have useful therapeutic value in ARDS and other pulmonary inflammatory diseases (Antonov et al., 2008). Several HSP90 inhibitors have been in clinical development as anticancer agents (Gao et al., 2019) and have advanced to phase 2 and 3 clinical trials. Some of these compounds could be readily available to become part of a therapeutic strategy for COVID-19 by possibly inhibiting SARS-COV-2 replication, reducing inflammation and protecting endothelial barrier function.

Limitations of the study

The major limitation of the study is the usage of epithelial cell lines, which might respond differently compared to epithelial cells in an organism, and intense data comparisons are necessary to define

physiologically relevant effects. Particularly, the high levels of viral RNA in some cells, which lead to induction of interferon and NF-kB target genes, might not be reached in epithelial cells in infected organisms (Nouailles et al., 2020). For the Hsp90 inhibitor, the effects described here need to be confirmed in animals and humans before clinical relevance can be attributed to this compound class.

Resource availability

Lead contact

Markus Landthaler, markus.landthaler@mdc-berlin.de.

Materials availability

No new reagents were created in this study.

Data and code availability

Raw sequencing data as well as count tables are for bulk and scRNA-seq experiments from cell lines are available at the Gene Expression Omnibus database (GEO), identifier GSE148729 (GEO: https://www.ncbi.nlm.nih.gov/geo/query/acc.cgi?acc=GSE148729). Supporting files are available on zenodo (Zen: Zenodo: https://zenodo.org/record/4031204#.YCpK_S1h1Bw).

METHODS

All methods can be found in the accompanying Transparent methods supplemental file.

SUPPLEMENTAL INFORMATION

Supplemental information can be found online at https://doi.org/10.1016/j.isci.2021.102151.

ACKNOWLEDGMENTS

The authors wish to thank Melanie Brinkmann, Leif Sander, Marco Hein, Joseph Luna, Friedemann Weber, and Robert Zinzen for comments and discussion; Jeannine Wilde, Tatiana Borodina, Daniele Franze, and Nouhad Benlasfer for sequencing and technical assistance; members of the Landthaler/Drosten/Rajewsky/Akalin/Selbach labs, Dan Munteanu and Alessandra Zappulo for continuous support under extraordinary circumstances; and numerous colleagues for feedback received via biorxiv.org or personal communications. This work was funded by BMBF grants scCoV2 (01KI20269) and NUM-COVID 19 Organo-Strat (01KX2021), and by the Berlin Institute of Health. Work in the T.F.M. laboratory was supported by the State of Schleswig-Holstein (Covid-19 DIO47)

AUTHOR CONTRIBUTIONS

E.W. performed experiments, analyzed data, and wrote the manuscript, K.M. performed infection and inhibitor experiments, V.F. performed coding and data analysis, A.D. performed smallRNA and total RNA sequencing together with S.A., and validation experiments for the miRNAs and vtRNAs, L.T.G. performed infection experiments and contributed to manuscript writing, R.A. performed experiments, F.K. analyzed small RNA and total RNA sequencing data together with I.L. and A.I., D.K. analyzed viral transcripts, K.H., K.Ho., T.F.M., and A.H. contributed AEC experiments, C.B. analyzed gene expression together with T.M., S.D.G. and J.P. performed experiments, S.P. contributed to designing and establishing single-cell experiments, D.N., M.A.M., M.A., A.A., N.R. supervised parts of the project, and C.D. and M.L. were responsible for overall supervision.

DECLARATION OF INTERESTS

The authors declare no competing interests.

Received: July 7, 2020
Revised: October 20, 2020
Accepted: February 2, 2021
Published: March 19, 2021

REFERENCES

Alhawiti, N.M., Al Mahri, S., Aziz, M.A., Malik, S.S., and Mohammad, S. (2017). TXNIP in metabolic regulation: physiological role and therapeutic outlook. Curr. Drug Targets *18*, 1095–1103.

Alsaadi, E.A.J., and Jones, I.M. (2019). Membrane binding proteins of coronaviruses. Future Virol. *14*, 275–286.

Angerer, P., Haghverdi, L., Buttner, M., Theis, F.J., Marr, C., and Buettner, F. (2016). destiny: diffusion maps for large-scale single-cell data in R. Bioinformatics *32*, 1241–1243.

Antonov, A., Snead, C., Gorshkov, B., Antonova, G.N., Verin, A.D., and Catravas, J.D. (2008). Heat shock protein 90 inhibitors protect and restore pulmonary endothelial barrier function. Am. J. Respir. Cell Mol. Biol. *39*, 551–559.

Aubry, L., Guetta, D., and Klein, G. (2009). The arrestin fold: variations on a theme. Curr. Genomics *10*, 133–142.

Badry, A., Jaspers, V.L.B., and Waugh, C.A. (2020). Environmental pollutants modulate RNA and DNA virus-activated miRNA-155 expression and innate immune system responses: insights into new immunomodulative mechanisms. J. Immunotoxicol. *17*, 86–93.

Bartel, D.P. (2004). MicroRNAs: genomics, biogenesis, mechanism, and function. Cell *116*, 281–297.

Bhattacharyya, S., and Vrati, S. (2015). The Malat1 long non-coding RNA is upregulated by signalling through the PERK axis of unfolded protein response during flavivirus infection. Sci. Rep. *5*, 17794.

Blanco-Melo, D., Nilsson-Payant, B.E., Liu, W., Uhl, S., Hoagland, D., Moller, R., Jordan, T.X., Oishi, K., Panis, M., Sachs, D., et al. (2020). Imbalanced host response to SARS-CoV-2 drives development of COVID-19. Cell *181*, 1036–1045.e9.

Bojkova, D., McGreig, J.E., McLaughlin, K.-M., Masterson, S.G., Widera, M., Krähling, V., Ciesek, S., Wass, M.N., Michaelis, M., and Cinatl, J. (2020). SARS-CoV-2 and SARS-CoV differ in their cell tropism and drug sensitivity profiles. Bioinformatics. https://doi.org/10.1093/bioinformatics/btab094.

Broemer, M., Krappmann, D., and Scheidereit, C. (2004). Requirement of Hsp90 activity for IkappaB kinase (IKK) biosynthesis and for constitutive and inducible IKK and NF-kappaB activation. Oncogene *23*, 5378–5386.

Buchrieser, J., Dufloo, J., Hubert, M., Monel, B., Planas, D., Rajah, M.M., Planchais, C., Porrot, F., Guivel-Benhassine, F., Van der Werf, S., et al. (2020). Syncytia formation by SARS-CoV-2-infected cells. EMBO J. *39*, e106267.

Butler, A., Hoffman, P., Smibert, P., Papalexi, E., and Satija, R. (2018). Integrating single-cell transcriptomic data across different conditions, technologies, and species. Nat. Biotechnol. *36*, 411–420.

Carrasco Pro, S., Dafonte Imedio, A., Santoso, C.S., Gan, K.A., Sewell, J.A., Martinez, M., Sereda, R., Mehta, S., and Fuxman Bass, J.I. (2018). Global landscape of mouse and human cytokine transcriptional regulation. Nucleic Acids Res. *46*, 9321–9337.

Channappanavar, R., and Perlman, S. (2017). Pathogenic human coronavirus infections: causes and consequences of cytokine storm and immunopathology. Semin. Immunopathol. *39*, 529–539.

Chu, H., Chan, J.F.-W., Yuen, T.T.-T., Shuai, H., Yuan, S., Wang, Y., Hu, B., Yip, C.C.-Y., Tsang, J.O.-L., Huang, X., et al. (2020). Comparative tropism, replication kinetics, and cell damage profiling of SARS-CoV-2 and SARS-CoV with implications for clinical manifestations, transmissibility, and laboratory studies of COVID-19: an observational study. Lancet Microbe. *1*, e14–e23.

Chua, R.L., Lukassen, S., Trump, S., Hennig, B.P., Wendisch, D., Pott, F., Debnath, O., Thurmann, L., Kurth, F., Volker, M.T., et al. (2020). COVID-19 severity correlates with airway epithelium-immune cell interactions identified by single-cell analysis. Nat. Biotechnol. *38*, 970–979.

Cristinelli, S., and Ciuffi, A. (2018). The use of single-cell RNA-Seq to understand virus-host interactions. Curr. Opin. Virol. *29*, 39–50.

Czerkies, M., Korwek, Z., Prus, W., Kochanczyk, M., Jaruszewicz-Blonska, J., Tudelska, K., Blonski, S., Kimmel, M., Brasier, A.R., and Lipniacki, T. (2018). Cell fate in antiviral response arises in the crosstalk of IRF, NF-kappaB and JAK/STAT pathways. Nat. Commun. *9*, 493.

De Deken, X., Corvilain, B., Dumont, J.E., and Miot, F. (2014). Roles of DUOX-mediated hydrogen peroxide in metabolism, host defense, and signaling. Antioxid. Redox Signal. *20*, 2776–2793.

DeDiego, M.L., Nieto-Torres, J.L., Jimenez-Guardeno, J.M., Regla-Nava, J.A., Alvarez, E., Oliveros, J.C., Zhao, J., Fett, C., Perlman, S., and Enjuanes, L. (2011). Severe acute respiratory syndrome coronavirus envelope protein regulates cell stress response and apoptosis. PLoS Pathog. *7*, e1002315.

Dickey, L.L., Hanley, T.M., Huffaker, T.B., Ramstead, A.G., O'Connell, R.M., and Lane, T.E. (2017). MicroRNA 155 and viral-induced neuroinflammation. J. Neuroimmunol. *308*, 17–24.

Dores, M.R., Lin, H., N, J.G., Mendez, F., and Trejo, J. (2015). The alpha-arrestin ARRDC3 mediates ALIX ubiquitination and G protein-coupled receptor lysosomal sorting. Mol. Biol. Cell *26*, 4660–4673.

Dowlatshahi, D.P., Sandrin, V., Vivona, S., Shaler, T.A., Kaiser, S.E., Melandri, F., Sundquist, W.I., and Kopito, R.R. (2012). ALIX is a Lys63-specific polyubiquitin binding protein that functions in retrovirus budding. Dev. Cell *23*, 1247–1254.

Drayman, N., Patel, P., Vistain, L., and Tay, S. (2019). HSV-1 single-cell analysis reveals the activation of anti-viral and developmental programs in distinct sub-populations. Elife *8*, e46339.

Duan, X., Han, Y., Yang, L., Nilsson, B., Wang, P., Zhang, T., Wang, X., Xu, D., Xiang, J.Z., uhl, s., et al. (2020). Identification of drugs blocking SARS-CoV-2 infection using human pluripotent stem cell-derived colonic organoids. bioRxiv, 2020.2005.2002.073320.

Elliott, E.I., and Sutterwala, F.S. (2015). Initiation and perpetuation of NLRP3 inflammasome activation and assembly. Immunol. Rev. *265*, 35–52.

Fehr, A.R., and Perlman, S. (2015). Coronaviruses: an overview of their replication and pathogenesis. Methods Mol. Biol. *1282*, 1–23.

Friedlander, M.R., Mackowiak, S.D., Li, N., Chen, W., and Rajewsky, N. (2012). miRDeep2 accurately identifies known and hundreds of novel microRNA genes in seven animal clades. Nucleic Acids Res. *40*, 37–52.

Frieman, M., Yount, B., Heise, M., Kopecky-Bromberg, S.A., Palese, P., and Baric, R.S. (2007). Severe acute respiratory syndrome coronavirus ORF6 antagonizes STAT1 function by sequestering nuclear import factors on the rough endoplasmic reticulum/Golgi membrane. J. Virol. *81*, 9812–9824.

Fung, T.S., Liao, Y., and Liu, D.X. (2016). Regulation of stress responses and translational control by coronavirus. Viruses *8*, 184.

Fung, T.S., and Liu, D.X. (2014). Coronavirus infection, ER stress, apoptosis and innate immunity. Front. Microbiol. *5*, 296.

Gao, C., Peng, Y.N., Wang, H.Z., Fang, S.L., Zhang, M., Zhao, Q., and Liu, J. (2019). Inhibition of heat shock protein 90 as a novel platform for the treatment of cancer. Curr. Pharm. Des. *25*, 849–855.

Gao, J., Xiao, S., Liu, X., Wang, L., Zhang, X., Ji, Q., Wang, Y., Mo, D., and Chen, Y. (2014). Inhibition of HSP90 attenuates porcine reproductive and respiratory syndrome virus production in vitro. Virol. J. *11*, 17.

Geller, R., Taguwa, S., and Frydman, J. (2012). Broad action of Hsp90 as a host chaperone required for viral replication. Biochim. Biophys. Acta *1823*, 698–706.

Gottwein, E. (2013). Roles of microRNAs in the life cycles of mammalian viruses. Curr. Top. Microbiol. Immunol. *371*, 201–227.

Gralinski, L.E., and Baric, R.S. (2015). Molecular pathology of emerging coronavirus infections. J. Pathol. *235*, 185–195.

Grandvaux, N., Servant, M.J., tenOever, B., Sen, G.C., Balachandran, S., Barber, G.N., Lin, R., and Hiscott, J. (2002). Transcriptional profiling of interferon regulatory factor 3 target genes: direct involvement in the regulation of interferon-stimulated genes. J. Virol. *76*, 5532–5539.

Guo, X., Zhang, M., Zhang, X., Tan, X., Guo, H., Zeng, W., Yan, G., Memon, A.M., Li, Z., Zhu, Y., et al. (2017). Porcine epidemic diarrhea virus induces autophagy to benefit its replication. Viruses *9*, 53.

Hackbart, M., Deng, X., and Baker, S.C. (2020). Coronavirus endoribonuclease targets viral polyuridine sequences to evade activating host sensors. Proc. Natl. Acad. Sci. U S A *117*, 8094–8103.

Haghverdi, L., Buttner, M., Wolf, F.A., Buettner, F., and Theis, F.J. (2016). Diffusion pseudotime robustly reconstructs lineage branching. Nat. Methods *13*, 845–848.

Hirano, T., and Murakami, M. (2020). COVID-19: a new virus, but a familiar receptor and cytokine release syndrome. Immunity *52*, 731–733.

Hoffmann, M., Kleine-Weber, H., Schroeder, S., Kruger, N., Herrler, T., Erichsen, S., Schiergens, T.S., Herrler, G., Wu, N.H., Nitsche, A., et al. (2020). SARS-CoV-2 cell entry depends on ACE2 and TMPRSS2 and is blocked by a clinically proven protease inhibitor. Cell *181*, 271–280.e8.

Horos, R., Buscher, M., Kleinendorst, R., Alleaume, A.M., Tarafder, A.K., Schwarzl, T., Dziuba, D., Tischer, C., Zielonka, E.M., Adak, A., et al. (2019). The small non-coding vault RNA1-1 acts as a riboregulator of autophagy. Cell *176*, 1054–1067.e2.

Imai-Matsushima, A., Martin-Sancho, L., Karlas, A., Imai, S., Zoranovic, T., Hocke, A.C., Mollenkopf, H.J., Berger, H., and Meyer, T.F. (2018). Long-term culture of distal airway epithelial cells allows differentiation towards alveolar epithelial cells suited for influenza virus studies. EBioMedicine *33*, 230–241.

Irigoyen, N., Firth, A.E., Jones, J.D., Chung, B.Y., Siddell, S.G., and Brierley, I. (2016). High-resolution analysis of coronavirus gene expression by RNA sequencing and ribosome profiling. PLoS Pathog. *12*, e1005473.

Iwanaszko, M., and Kimmel, M. (2015). NF-kappaB and IRF pathways: cross-regulation on target genes promoter level. BMC Genomics *16*, 307.

Katoh, H., Kubota, T., Nakatsu, Y., Tahara, M., Kidokoro, M., and Takeda, M. (2017). Heat shock protein 90 ensures efficient mumps virus replication by assisting with viral polymerase complex formation. J. Virol. *91*, e02220-16.

Kemp, V., Laconi, A., Cocciolo, G., Berends, A.J., Breit, T.M., and Verheije, M.H. (2020). miRNA repertoire and host immune factor regulation upon avian coronavirus infection in eggs. Arch. Virol. *165*, 835–843.

Kim, D., Lee, J.-Y., Yang, J.-S., Kim, J.W., Kim, V.N., and Chang, H. (2020). The architecture of SARS-CoV-2 transcriptome. Cell *181*, 914–921.e10.

Kindler, E., Thiel, V., and Weber, F. (2016). Interaction of SARS and MERS Coronaviruses with the Antiviral Interferon Response. Adv. Virus Res. *96*, 219–243.

Klann, K., Bojkova, D., Tascher, G., Ciesek, S., Munch, C., and Cinatl, J. (2020). Growth factor receptor signaling inhibition prevents SARS-CoV-2 replication. Mol. Cell *80*, 164–174.e4.

La Manno, G., Soldatov, R., Zeisel, A., Braun, E., Hochgerner, H., Petukhov, V., Lidschreiber, K., Kastriti, M.E., Lonnerberg, P., Furlan, A., et al. (2018). RNA velocity of single cells. Nature *560*, 494–498.

Lamers, M.M., Beumer, J., van der Vaart, J., Knoops, K., Puschhof, J., Breugem, T.I., Ravelli, R.B.G., Paul van Schayck, J., Mykytyn, A.Z., Duimel, H.Q., et al. (2020). SARS-CoV-2 productively infects human gut enterocytes. Science *369*, 50–54.

Lee, J.E., Morrison, W., and Hollien, J. (2018). Hairy and enhancer of split 1 (HES1) protects cells from endoplasmic reticulum stress-induced apoptosis through repression of GADD34. J. Biol. Chem. *293*, 5947–5955.

Leon-Icaza, S.A., Zeng, M., and Rosas-Taraco, A.G. (2019). microRNAs in viral acute respiratory infections: immune regulation, biomarkers, therapy, and vaccines. ExRNA *1*, 1.

Li, S., Yuan, L., Dai, G., Chen, R.A., Liu, D.X., and Fung, T.S. (2019). Regulation of the ER stress response by the ion channel activity of the infectious bronchitis coronavirus envelope protein modulates virion release, apoptosis, viral fitness, and pathogenesis. Front. Microbiol. *10*, 3022.

Li, Y.-H., Tao, P.-Z., Liu, Y.-Z., and Jiang, J.-D. (2004). Geldanamycin, a Ligand of heat shock protein 90, inhibits the replication of herpes simplex virus type 1 in vitro. Antimicrob. Agents Chemother. *48*, 867.

Liao, M., Liu, Y., Yuan, J., Wen, Y., Xu, G., Zhao, J., Cheng, L., Li, J., Wang, X., Wang, F., et al. (2020). Single-cell landscape of bronchoalveolar immune cells in patients with COVID-19. Nat. Med. *26*, 842–844.

Liu, S.Y., Aliyari, R., Chikere, K., Li, G., Marsden, M.D., Smith, J.K., Pernet, O., Guo, H., Nusbaum, R., Zack, J.A., et al. (2013). Interferon-inducible cholesterol-25-hydroxylase broadly inhibits viral entry by production of 25-hydroxycholesterol. Immunity *38*, 92–105.

Marcu, M.G., Doyle, M., Bertolotti, A., Ron, D., Hendershot, L., and Neckers, L. (2002). Heat shock protein 90 modulates the unfolded protein response by stabilizing IRE1alpha. Mol. Cell. Biol. *22*, 8506–8513.

Masters, P.S. (2006). The molecular biology of coronaviruses. Adv. Virus Res. *66*, 193–292.

Masters, P.S., and Perlman, S. (2013). Coronaviridae. In Fields Virology, D.M. Knipe and P.M. Howley, eds. (Wolters Kluwer Health/ Lippincott Williams & Wilkins), pp. 825–884.

Mehta, A., and Baltimore, D. (2016). MicroRNAs as regulatory elements in immune system logic. Nat. Rev. Immunol. *16*, 279–294.

Menachery, V.D., Debbink, K., and Baric, R.S. (2014a). Coronavirus non-structural protein 16: evasion, attenuation, and possible treatments. Virus Res. *194*, 191–199.

Menachery, V.D., Eisfeld, A.J., Schafer, A., Josset, L., Sims, A.C., Proll, S., Fan, S., Li, C., Neumann, G., Tilton, S.C., et al. (2014b). Pathogenic influenza viruses and coronaviruses utilize similar and contrasting approaches to control interferon-stimulated gene responses. mBio *5*, e01174-14.

Moore, B.J.B., and June, C.H. (2020). Cytokine release syndrome in severe COVID-19. Science *368*, 473–547.

Muller, M.A., van der Hoek, L., Voss, D., Bader, O., Lehmann, D., Schulz, A.R., Kallies, S., Suliman, T., Fielding, B.C., Drosten, C., et al. (2010). Human coronavirus NL63 open reading frame 3 encodes a virion-incorporated N-glycosylated membrane protein. Virol. J. *7*, 6.

Narayanan, K., Huang, C., and Makino, S. (2008). SARS coronavirus accessory proteins. Virus Res. *133*, 113–121.

Nouailles, G., Wyler, E., Pennitz, P., Postmus, D., Vladimirova, D., Kazmierski, J., Pott, F., Dietert, K., Mülleder, M., Farztdinov, V., et al. (2020). Longitudinal omics in Syrian hamsters integrated with human data unravel complexity of moderate immune responses to SARS-CoV-2. bioRxiv, 2020.2012.2018.423524.

Onabajo, O.O., Banday, A.R., Stanifer, M.L., Yan, W., Obajemu, A., Santer, D.M., Florez-Vargas, O., Piontkivska, H., Vargas, J.M., Ring, T.J., et al. (2020). Interferons and viruses induce a novel truncated ACE2 isoform and not the full-length SARS-CoV-2 receptor. Nat. Genet. *52*, 1283–1293.

Oslowski, C.M., Hara, T., O'Sullivan-Murphy, B., Kanekura, K., Lu, S., Hara, M., Ishigaki, S., Zhu, L.J., Hayashi, E., Hui, S.T., et al. (2012). Thioredoxin-interacting protein mediates ER stress-induced beta cell death through initiation of the inflammasome. Cell Metab. *16*, 265–273.

Persson, H., Kvist, A., Vallon-Christersson, J., Medstrand, P., Borg, A., and Rovira, C. (2009). The non-coding RNA of the multidrug resistance-linked vault particle encodes multiple regulatory small RNAs. Nat. Cell Biol. *11*, 1268–1271.

Reigel, F. (1985). Isolation of human pathogenic viruses from clinical material on CaCo2 cells. J. Virol. Methods *12*, 323–327.

Russell, A.B., Trapnell, C., and Bloom, J.D. (2018). Extreme heterogeneity of influenza virus infection in single cells. Elife *7*, e32303.

Santoro, M.G., Amici, C., and Rossi, A. (2010). Role of heat shock proteins in viral infection. In Prokaryotic and Eukaryotic Heat Shock Proteins in Infectious Disease, A.G. Pockley, S.K. Calderwood, and M.G. Santoro, eds. (Springer Netherlands), pp. 51–84.

Schneider, W.M., Chevillotte, M.D., and Rice, C.M. (2014). Interferon-stimulated genes: a complex web of host defenses. Annu. Rev. Immunol. *32*, 513–545.

Schoggins, J.W. (2019). Interferon-stimulated genes: what do they all do? Annu. Rev. Virol. *6*, 567–584.

Shnayder, M., Nachshon, A., Krishna, B., Poole, E., Boshkov, A., Binyamin, A., Maza, I., Sinclair, J., Schwartz, M., and Stern-Ginossar, N. (2018). Defining the transcriptional landscape during cytomegalovirus latency with single-cell RNA sequencing. MBio *9*, e00013-18.

Sola, I., Almazan, F., Zuniga, S., and Enjuanes, L. (2015). Continuous and discontinuous RNA synthesis in coronaviruses. Annu. Rev. Virol. *2*, 265–288.

Spiegel, M., Pichlmair, A., Martinez-Sobrido, L., Cros, J., Garcia-Sastre, A., Haller, O., and Weber, F. (2005). Inhibition of Beta interferon induction by severe acute respiratory syndrome coronavirus suggests a two-step model for activation of interferon regulatory factor 3. J. Virol. *79*, 2079–2086.

Stanifer, M.L., Kee, C., Cortese, M., Zumaran, C.M., Triana, S., Mukenhirn, M., Kraeusslich, H.G., Alexandrov, T., Bartenschlager, R., and Boulant, S. (2020). Critical role of type III interferon in controlling SARS-CoV-2 infection in human intestinal epithelial cells. Cell Rep. *32*, 107863.

Sultan, I., Howard, S., and Tbakhi, A. (2020). Drug Repositioning suggests a role for the heat shock protein 90 inhibitor geldanamycin in treating COVID-19 infection. ResearchSquare. https://www.researchsquare.com/article/rs-18714/v1.

Taiaroa, G., Rawlinson, D., Featherstone, L., Pitt, M., Caly, L., Druce, J., Purcell, D., Harty, L., Tran, T., Roberts, J., et al. (2020). Direct RNA sequencing and early evolution of SARS-CoV-2. bioRxiv, 2020.2003.2005.976167.

Thai, T.H., Calado, D.P., Casola, S., Ansel, K.M., Xiao, C., Xue, Y., Murphy, A., Frendewey, D., Valenzuela, D., Kutok, J.L., et al. (2007). Regulation of the germinal center response by microRNA-155. Science *316*, 604–608.

Thepparit, C., Khongwichit, S., Ketsuwan, K., Libsittikul, S., Auewarakul, P., and Smith, D.R. (2019). Dengue virus requires apoptosis linked gene-2-interacting protein X (ALIX) for viral propagation. Virus Res. *261*, 65–71.

Thomson, D.W., Pillman, K.A., Anderson, M.L., Lawrence, D.M., Toubia, J., Goodall, G.J., and Bracken, C.P. (2015). Assessing the gene regulatory properties of Argonaute-bound small RNAs of diverse genomic origin. Nucleic Acids Res. *43*, 470–481.

V'kovski, P., Gultom, M., Steiner, S., Kelly, J., Russeil, J., Mangeat, B., Cora, E., Pezoldt, J., Holwerda, M., Kratzel, A., et al. (2020). Disparate temperature-dependent virus – host dynamics for SARS-CoV-2 and SARS-CoV in the human respiratory epithelium. bioRxiv, 2020.2004.2027.062315.

van Hemert, M.J., van den Worm, S.H., Knoops, K., Mommaas, A.M., Gorbalenya, A.E., and Snijder, E.J. (2008). SARS-coronavirus replication/transcription complexes are membrane-protected and need a host factor for activity in vitro. PLoS Pathog. *4*, e1000054.

Versteeg, G.A., van de Nes, P.S., Bredenbeek, P.J., and Spaan, W.J. (2007). The coronavirus spike protein induces endoplasmic reticulum stress and upregulation of intracellular chemokine mRNA concentrations. J. Virol. *81*, 10981–10990.

Viehweger, A., Krautwurst, S., Lamkiewicz, K., Madhugiri, R., Ziebuhr, J., Holzer, M., and Marz, M. (2019). Direct RNA nanopore sequencing of full-length coronavirus genomes provides novel insights into structural variants and enables modification analysis. Genome Res. *29*, 1545–1554.

Woods, P.S., Doolittle, L.M., Rosas, L.E., Nana-Sinkam, S.P., Tili, E., and Davis, I.C. (2020). Increased expression of microRNA-155-5p by alveolar type II cells contributes to development of lethal ARDS in H1N1 influenza A virus-infected mice. Virology *545*, 40–52.

World Health Organization. (2020). Coronavirus Disease (COVID-19) Pandemic (WHO). https://www.who.int/emergencies/diseases/novel-coronavirus-2019.

Wyler, E., Franke, V., Menegatti, J., Kocks, C., Boltengagen, A., Praktiknjo, S., Walch-Ruckheim, B., Bosse, J., Rajewsky, N., Grasser, F., et al. (2019). Single-cell RNA-sequencing of herpes simplex virus 1-infected cells connects NRF2 activation to an antiviral program. Nat. Commun. *10*, 4878.

Xiong, Y., Liu, Y., Cao, L., Wang, D., Guo, M., Jiang, A., Guo, D., Hu, W., Yang, J., Tang, Z., et al. (2020). Transcriptomic characteristics of bronchoalveolar lavage fluid and peripheral blood mononuclear cells in COVID-19 patients. Emerg. Microbes Infect. *9*, 761–770.

Yoshikawa, T., Hill, T.E., Yoshikawa, N., Popov, V.L., Galindo, C.L., Garner, H.R., Peters, C.J., and Tseng, C.T. (2010). Dynamic innate immune responses of human bronchial epithelial cells to severe acute respiratory syndrome-associated coronavirus infection. PLoS One *5*, e8729.

Zanini, F., Pu, S.Y., Bekerman, E., Einav, S., and Quake, S.R. (2018). Single-cell transcriptional dynamics of flavivirus infection. Elife *7*, e32942.

Zeng, F.R., Tang, L.J., He, Y., and Garcia, R.C. (2015). An update on the role of miRNA-155 in pathogenic microbial infections. Microbes Infect *17*, 613–621.

Zhou, H., Huang, X., Cui, H., Luo, X., Tang, Y., Chen, S., Wu, L., and Shen, N. (2010). miR-155 and its star-form partner miR-155* cooperatively regulate type I interferon production by human plasmacytoid dendritic cells. Blood *116*, 5885–5894.

Ziegler, C.G.K., Allon, S.J., Nyquist, S.K., Mbano, I.M., Miao, V.N., Tzouanas, C.N., Cao, Y., Yousif, A.S., Bals, J., Hauser, B.M., et al. (2020). SARS-CoV-2 receptor ACE2 is an interferon-stimulated gene in human airway epithelial cells and is detected in specific cell subsets across tissues. Cell *181*, 1016–1035.e19.

Zuehlke, A.D., Beebe, K., Neckers, L., and Prince, T. (2015). Regulation and function of the human HSP90AA1 gene. Gene *570*, 8–16.

iScience, Volume *24*

Supplemental Information

Transcriptomic profiling of SARS-CoV-2 infected human cell lines identifies HSP90 as target for COVID-19 therapy

Emanuel Wyler, Kirstin Mösbauer, Vedran Franke, Asija Diag, Lina Theresa Gottula, Roberto Arsiè, Filippos Klironomos, David Koppstein, Katja Hönzke, Salah Ayoub, Christopher Buccitelli, Karen Hoffmann, Anja Richter, Ivano Legnini, Andranik Ivanov, Tommaso Mari, Simone Del Giudice, Jan Papies, Samantha Praktiknjo, Thomas F. Meyer, Marcel Alexander Müller, Daniela Niemeyer, Andreas Hocke, Matthias Selbach, Altuna Akalin, Nikolaus Rajewsky, Christian Drosten, and Markus Landthaler

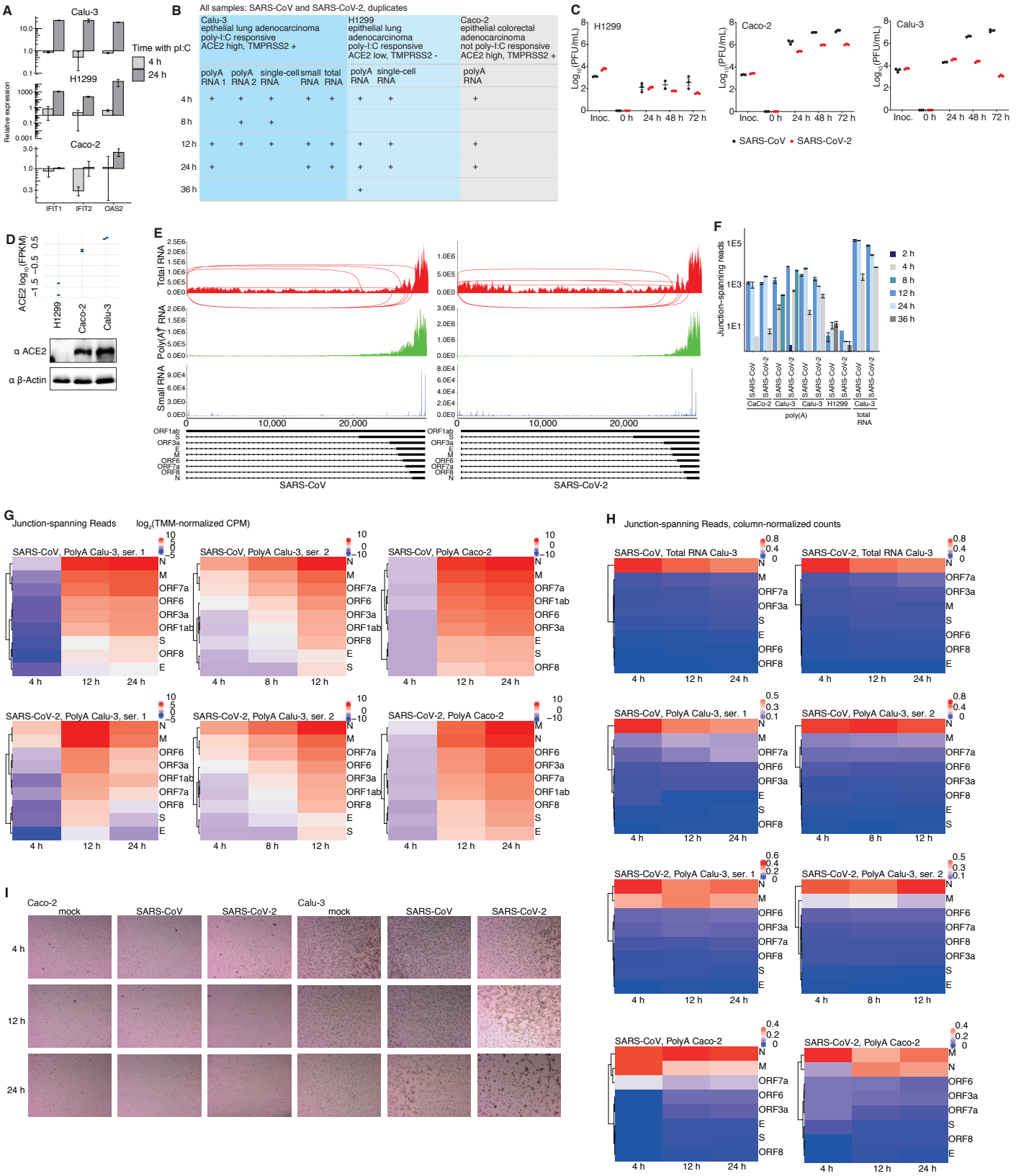

Figure S1. Different permissiveness of SARS-CoV/-2 infection in cell lines, Related to Figure 1

A, Relative quantification (RQ) of responsiveness to dsRNA of the cell lines as tested by RT-qPCR of three ISGs upon transfection of poly-I:C.

B, Overview of experimental set up and collected datasets. Calu-3 cells turned out to be the most suitable cell line.

C, Growth kinetics of SARS-CoV and SARS-CoV-2 in the different cell lines (MOI 0.01). Log10 of plaque forming units (PFU) of the inoculum (inoc.) and different hours post infection are plotted.

D, Expression values of the ACE2 mRNA in the polyA RNA-seq mock samples (upper part) and protein expression assessed by Western blot analysis with specific antibodies of indicated cell lines (lower part). H1299 cells showed neither mRNA nor protein expression of ACE2.

E, Coverage across the viral genome merged across all datasets for total RNA-seq, poly(A)+ RNA-seq, and small RNA-seq data. The top eight junctions supported by split reads are plotted in “sashimi” style for the total RNA-seq.

F, Barplot of junction-spanning reads from poly(A) and total RNAseq at indicated time point of different cell lines and series.

G and H, Heatmaps of canonical junction-spanning reads, averaged across biological replicates per time point, expressed in TMM-normalized counts per million (G), or relative counts per time point (H). ORF1ab levels are estimated by counting contiguous reads mapping to the leader junction site.

I, Phase-contrast microscopy images of with either virus infected Caco-2 and Calu-3 cells at indicated time points. CaCo-2 cells appear hardly affected by the infection; whereas, Calu-3 clearly show signs of cell death at 24 hours post infection (hpi), particularly when infected with SARS-CoV-2.

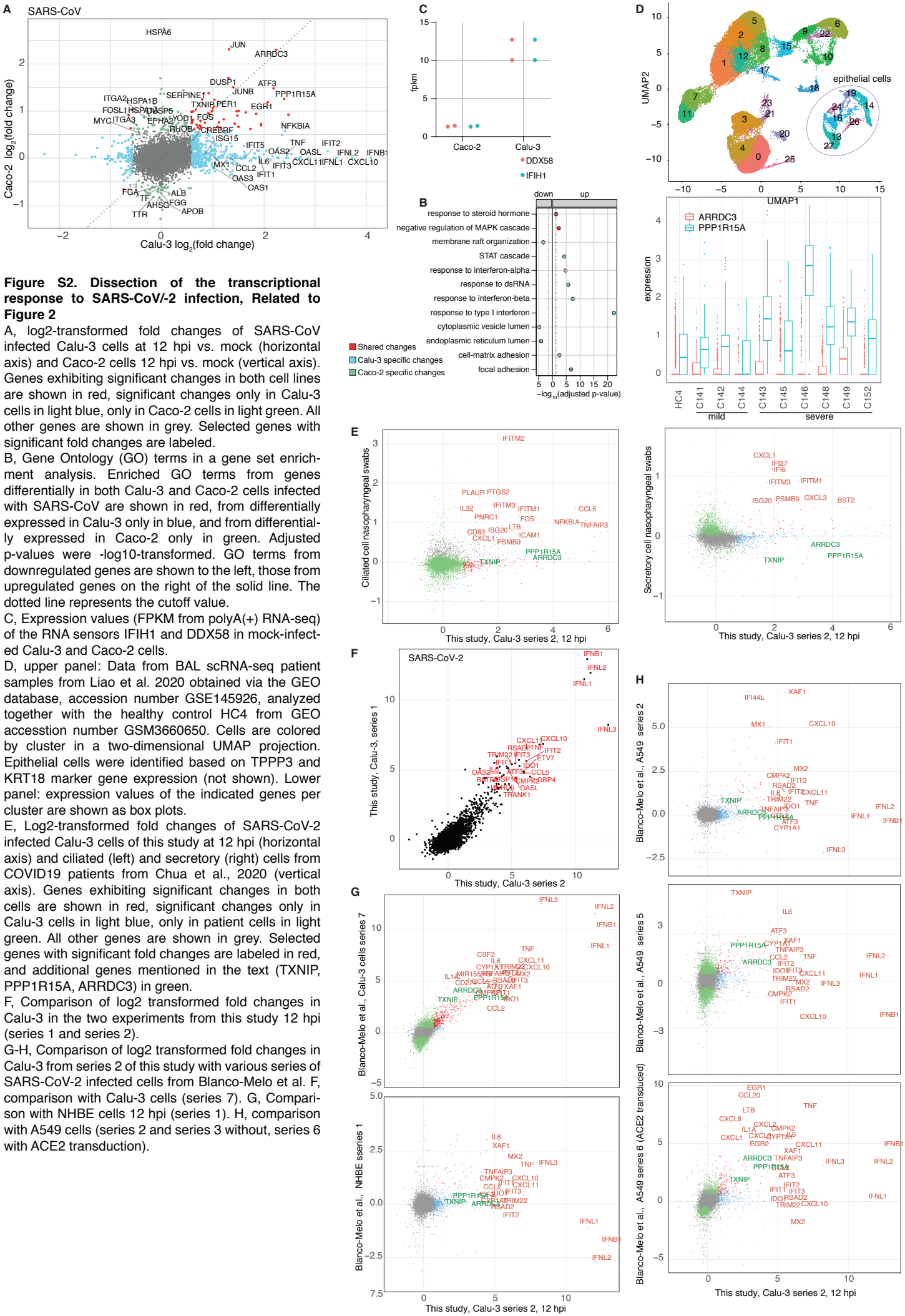

Figure S2. Dissection of the transcriptional response to SARS-CoV/-2 infection, Related to Figure 2

A, log2-transformed fold changes of SARS-CoV infected Calu-3 cells at 12 hpi vs. mock (horizontal axis) and Caco-2 cells 12 hpi vs. mock (vertical axis). Genes exhibiting significant changes in both cell lines are shown in red, significant changes only in Calu-3 cells in light blue, only in Caco-2 cells in light green. All other genes are shown in grey. Selected genes with significant fold changes are labeled.

B, Gene Ontology (GO) terms in a gene set enrichment analysis. Enriched GO terms from genes differentially in both Calu-3 and Caco-2 cells infected with SARS-CoV are shown in red, from differentially expressed in Calu-3 only in blue, and from differentially expressed in Caco-2 only in green. Adjusted p-values were -log10-transformed. GO terms from downregulated genes are shown to the left, those from upregulated genes on the right of the solid line. The dotted line represents the cutoff value.

C, Expression values (FPKM from polyA(+) RNA-seq) of the RNA sensors IFIH1 and DDX58 in mock-infected Calu-3 and Caco-2 cells.

D, upper panel: Data from BAL scRNA-seq patient samples from Liao et al. 2020 obtained via the GEO database, accession number GSE145926, analyzed together with the healthy control HC4 from GEO accesstion number GSM3660650. Cells are colored by cluster in a two-dimensional UMAP projection. Epithelial cells were identified based on TPPP3 and KRT18 marker gene expression (not shown). Lower panel: expression values of the indicated genes per cluster are shown as box plots.

E, Log2-transformed fold changes of SARS-CoV-2 infected Calu-3 cells of this study at 12 hpi (horizontal axis) and ciliated (left) and secretory (right) cells from COVID19 patients from Chua et al., 2020 (vertical axis). Genes exhibiting significant changes in both cells are shown in red, significant changes only in Calu-3 cells in light blue, only in patient cells in light green. All other genes are shown in grey. Selected genes with significant fold changes are labeled in red, and additional genes mentioned in the text (TXNIP, PPP1R15A, ARRDC3) in green.

F, Comparison of log2 transformed fold changes in Calu-3 in the two experiments from this study 12 hpi (series 1 and series 2).

G-H, Comparison of log2 transformed fold changes in Calu-3 from series 2 of this study with various series of SARS-CoV-2 infected cells from Blanco-Melo et al. F, comparison with Calu-3 cells (series 7). G, Comparison with NHBE cells 12 hpi (series 1). H, comparison with A549 cells (series 2 and series 3 without, series 6 with ACE2 transduction).

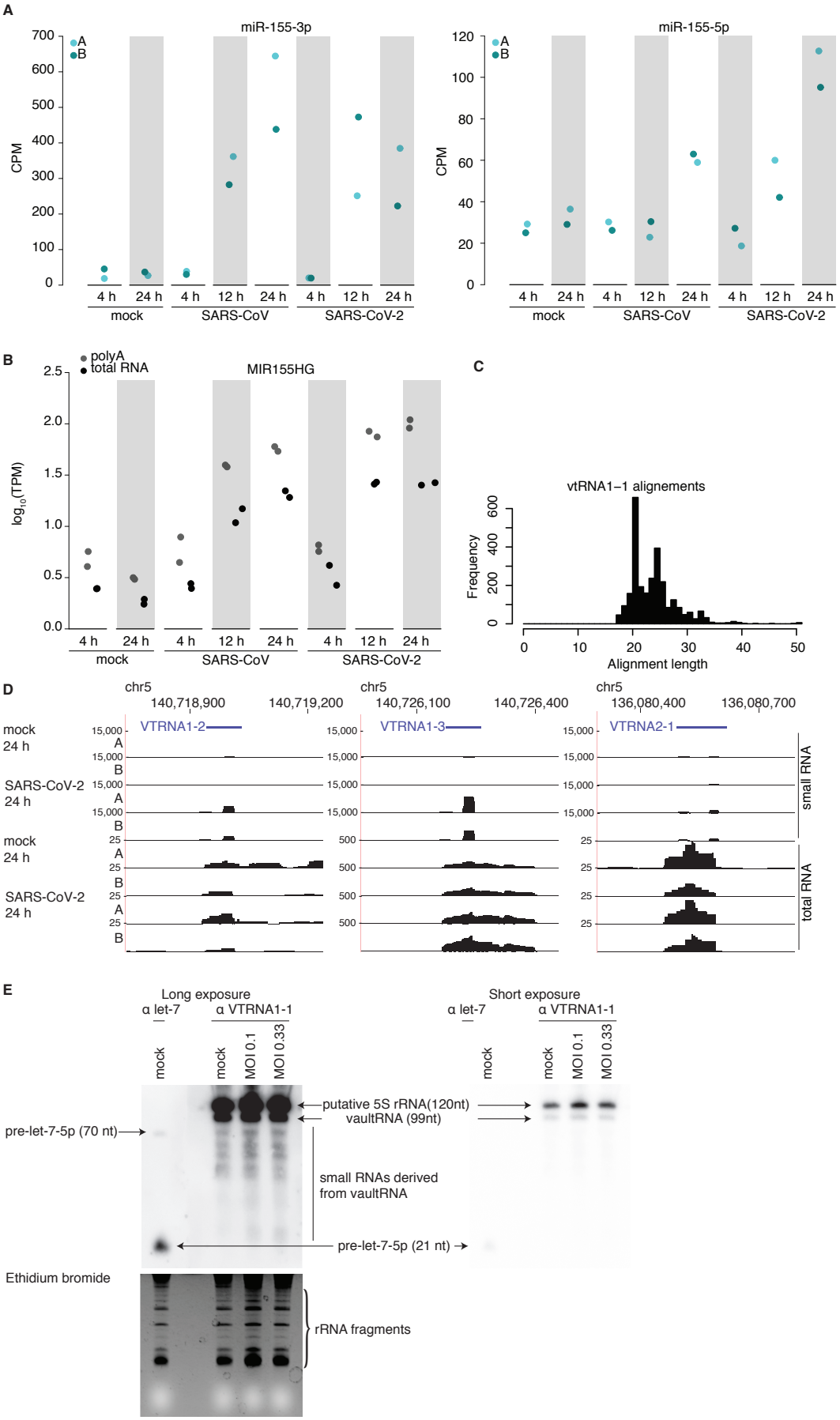

Figure S3. MicroRNA miR-155 and vaultRNA-derived miRNAs are induced by the infection, Related to Figure 3
A, Normalized counts (counts per million) of miR-155-3p (left panel) and miR-155-5p (right panel), colored by replicate.
B, Log10 miRNA-155 host gene transcripts per million in samples measured by polyA- or total RNAseq.
C, length distribution of small RNAs aligning to the VTRNA1-1 locus
D, coverage plots of the three vaultRNA genes VTRNA1-2, VTRNA1-3, and VTRNA2-1.
E, validation of small RNAs from the VTRNA1-1 locus using Northern blotting of SARS-CoV-2 infected Calu-3 cells 24 hpi. Input 5 μg total RNA. Left panel: probing with probes recognizing let-7-5p (left lane) and vtRNAs (three lanes on the right. Predicted sizes are indicated. The strong band above the vtRNA likely represents 5S/5.8S rRNA. Right panel: same as left panel, but short exposure to visualize vtRNA1-1 levels. Botttom: Ethidium bromide staining as loading control with tRNA with predicted size indicated.

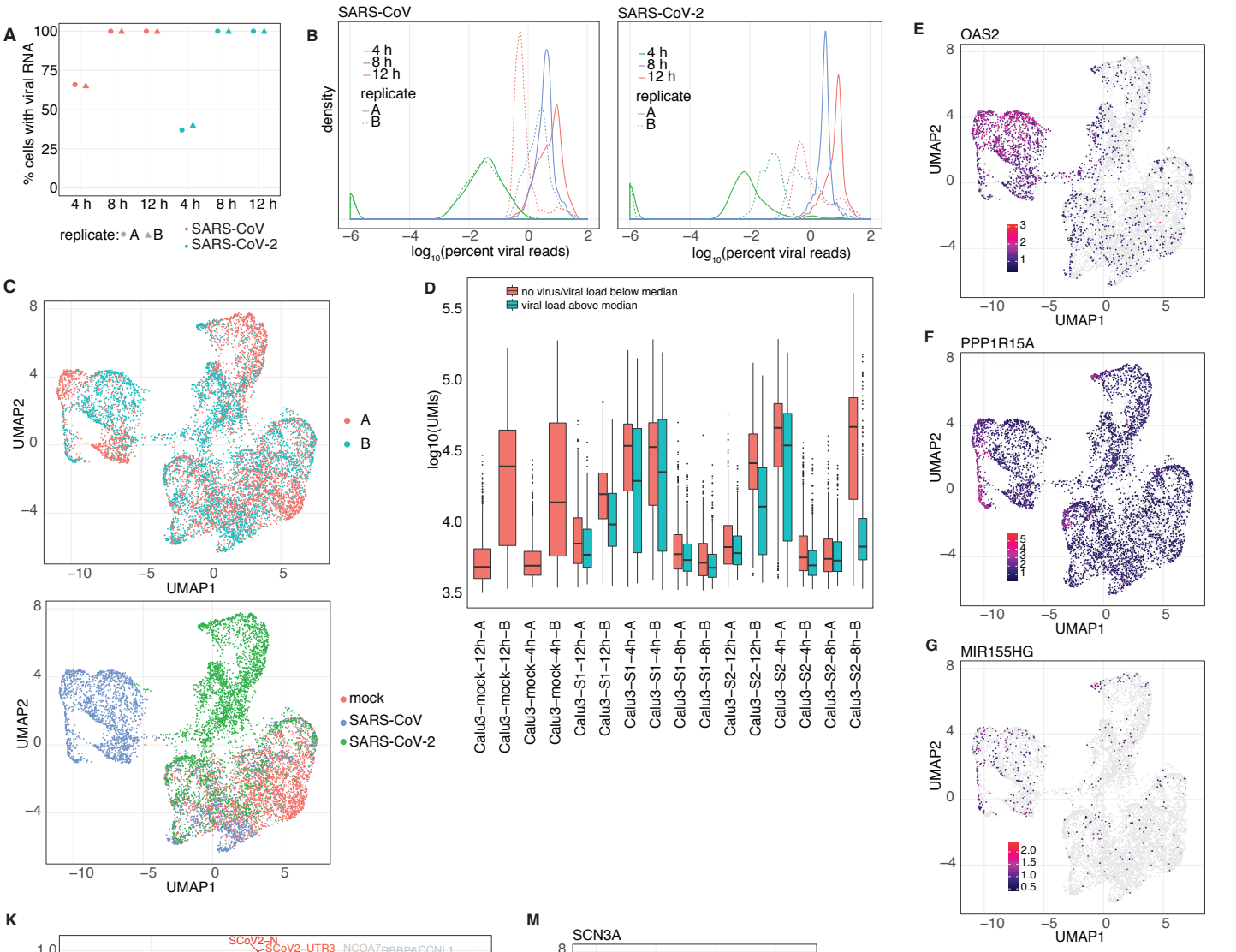

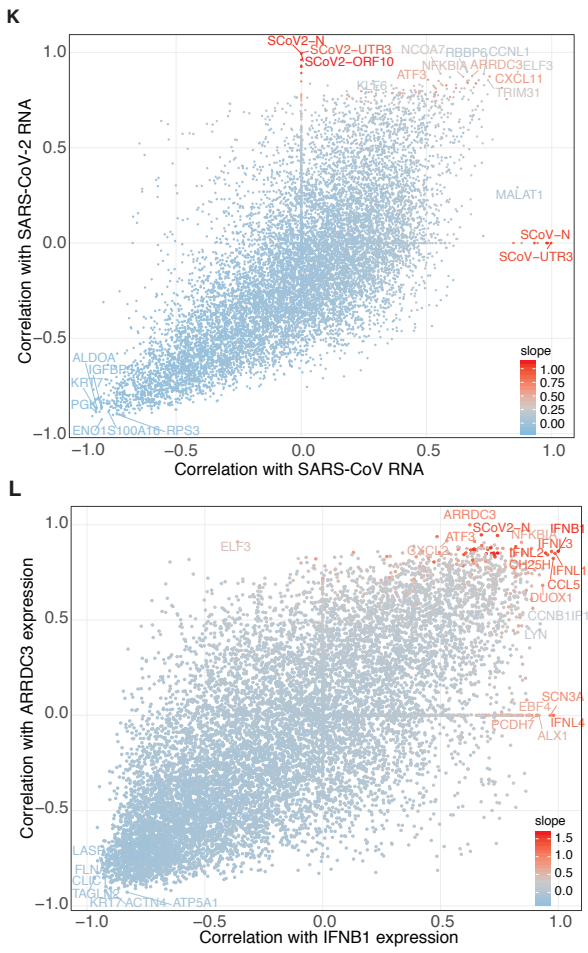

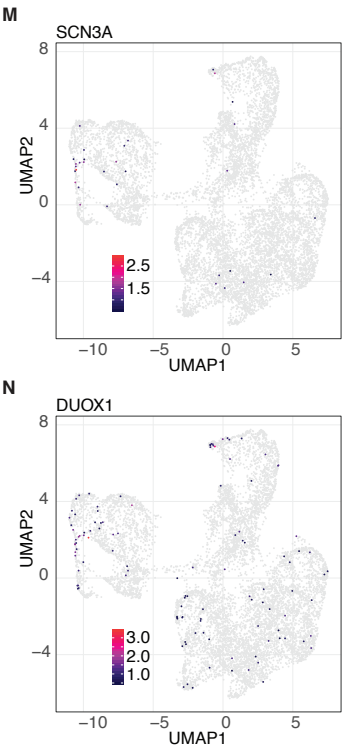

Figure S4. Single-cell RNA-sequencing shows different expression dynamics of genes induced by infection, Related to Figure 4

A, Percentages of cells bearing viral transcripts.

B, Relative densities of the percentage of viral transcripts per cell (log10 transformed) for SARS-CoV (left) and SARS-CoV-2 infected cells (right).

C, Projection as in Figure 4, with cells colored by replicate (upper panel) and type of infection (lower panel).

D, Cells from infected samples were split into groups with the amount of viral RNA either above (petrol) or below (red) the median. RNA molecule counts (UMI, unique molecular identifiers) were then displayed per group as boxplots. Median is shown as thick black line, lower and upper hinges correspond to the first and third quartiles, and whiskers to 1.5 times the inter-quartile range.

E-G, Projection as in Figure 4, but colored by expression values of the indicated genes.

K, Correlation of gene expression values with the amount of SARS-CoV RNA (x-axis) and SARS-CoV-2 RNA (y-axis).

L, Correlation of gene expression values with the amount of IFNB1 (x-axis) and ARRDC3 (y-axis).

M, N, Projection as in Figure 4, but colored by expression values of the indicated genes.

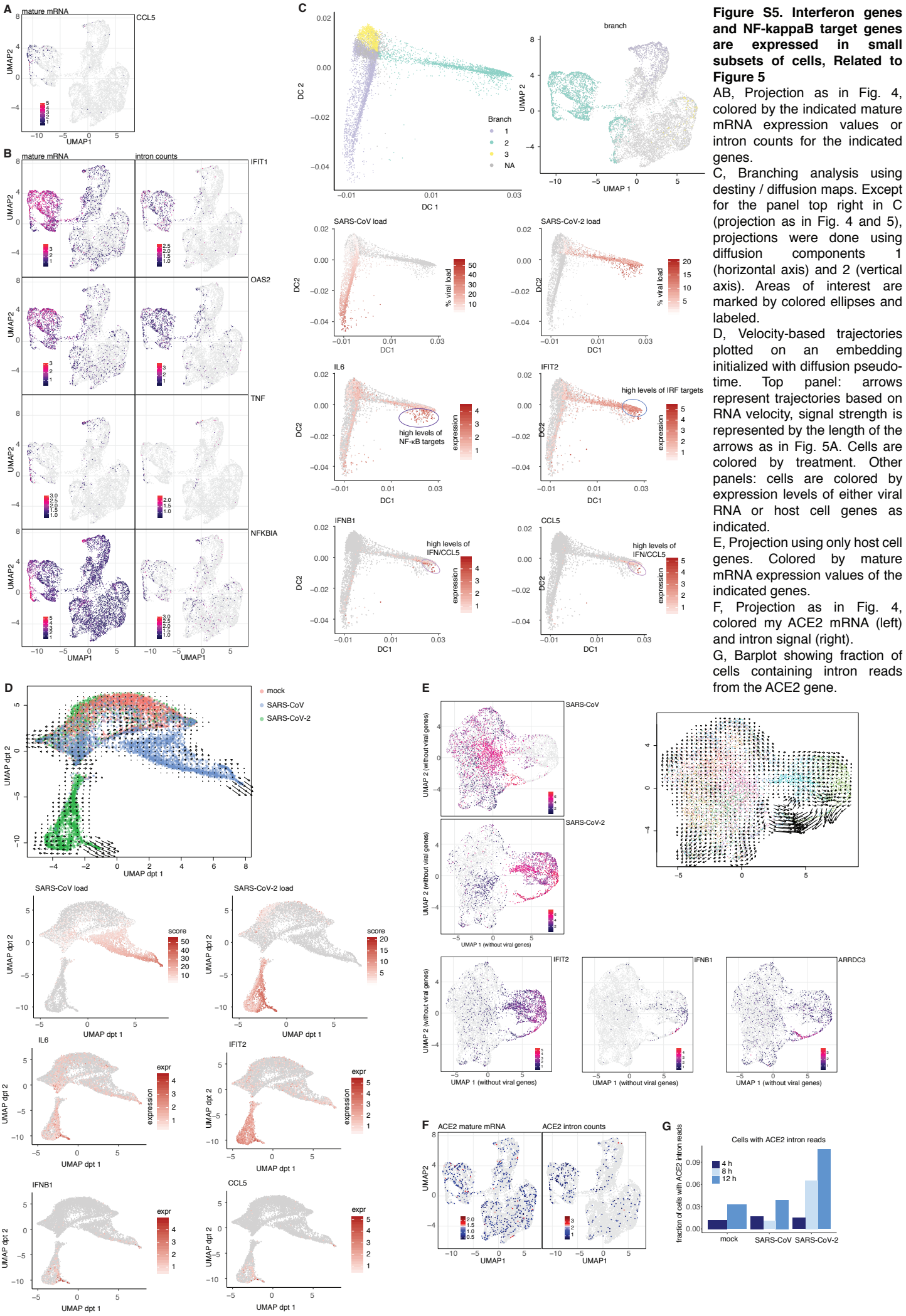

Figure S5. Interferon genes and NF-kappaB target genes are expressed in small subsets of cells, Related to Figure 5

AB, Projection as in Fig. 4, colored by the indicated mature mRNA expression values or intron counts for the indicated genes.

C, Branching analysis using destiny / diffusion maps. Except for the panel top right in C (projection as in Fig. 4 and 5), projections were done using diffusion components 1 (horizontal axis) and 2 (vertical axis). Areas of interest are marked by colored ellipses and labeled.

D, Velocity-based trajectories plotted on an embedding initialized with diffusion pseudotime. Top panel: arrows represent trajectories based on RNA velocity, signal strength is represented by the length of the arrows as in Fig. 5A. Cells are colored by treatment. Other panels: cells are colored by expression levels of either viral RNA or host cell genes as indicated.

E, Projection using only host cell genes. Colored by mature mRNA expression values of the indicated genes.

F, Projection as in Fig. 4, colored my ACE2 mRNA (left) and intron signal (right).

G, Barplot showing fraction of cells containing intron reads from the ACE2 gene.

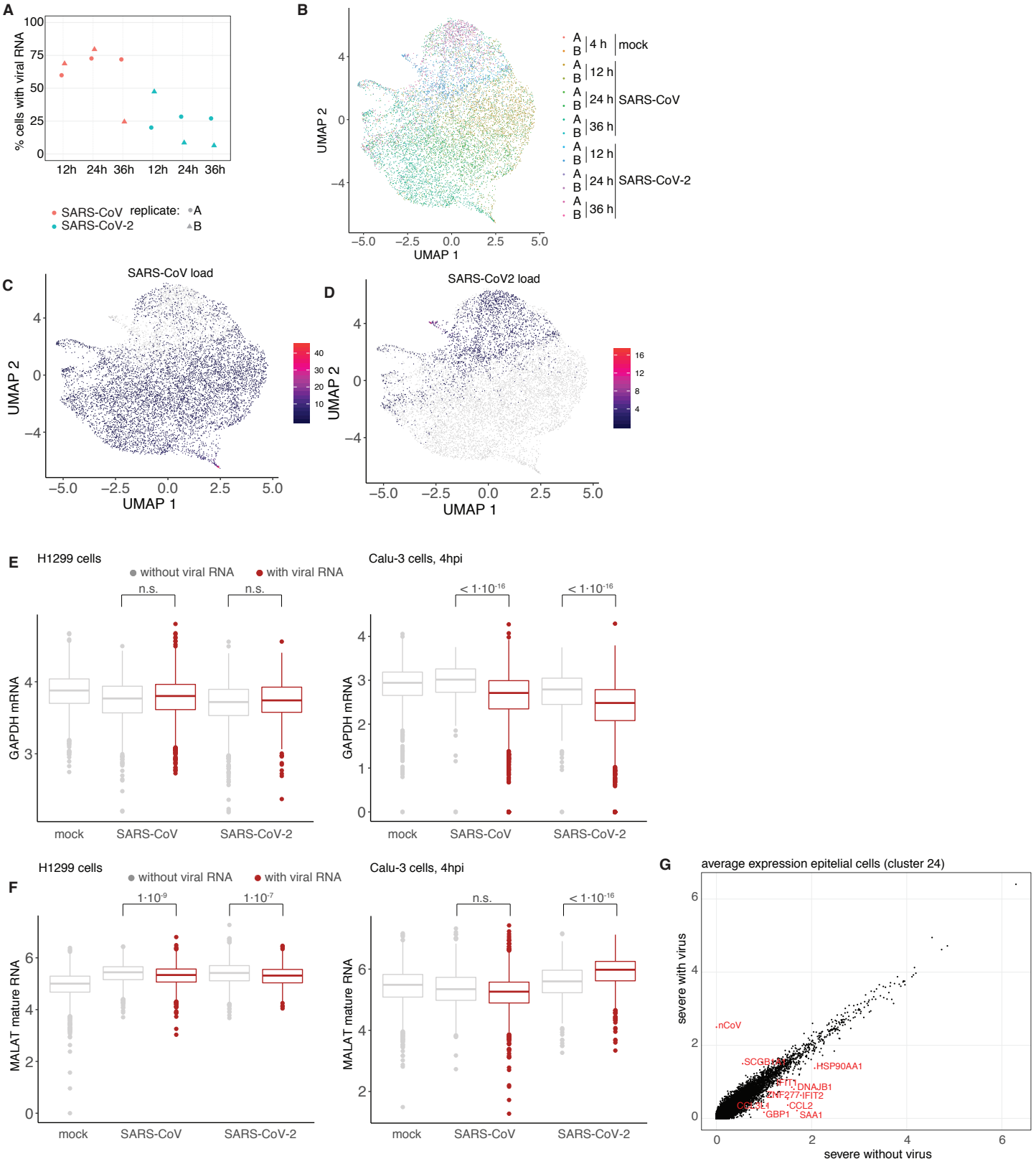

Figure S6. HSP90AA1 is deregulated in SARS-CoV-2 infected cells, Related to Figure 6

A, Percentages of cells with virus in the H1299 scRNA-seq data.

B-D, H1299 cells are projected in two dimensions using Uniform Manifold Approximation and Projection (UMAP) and colored as indicated.

EF, as in Fig. 6B and D, but for GAPDH and MALAT1 transcripts.

G, average gene expression values in epithelial cells/cluster 24 (see Supplementary Figure 2) of cells with and without viral reads. Expression of viral reads is represented by “nCoV”.

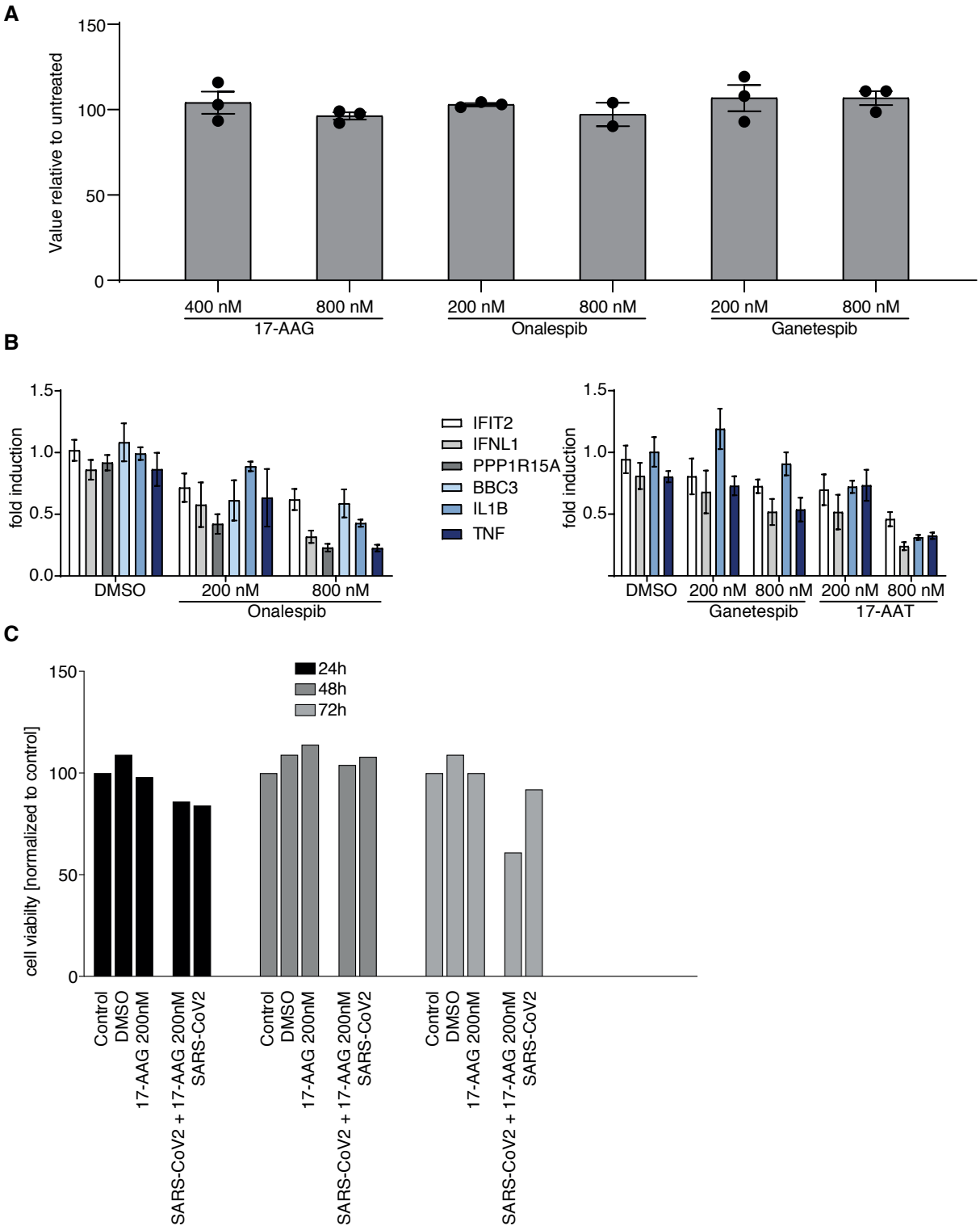

Figure S7. HSP90 inhibitors treatment reduce SARS-CoV-2 replication and induction of pro-inflammatory cytokines, Related to Figure 7
A, Cytotoxicity assay (CellTiter-Glo) of cells treated with the indicated HSP90 inhibitors for 16 hours.
B, Expression levels of selected mRNAs from the samples shown in Fig. 7 probed by RT-qPCR.
C, Cytotoxicity assay (CellTiter-Glo) of AECs treated with indicated treatments and time points.

Table S1, Related to Figure 1
Overview of datasets
Within file names, S1 means SARS-CoV-1 infection, S2 means SARS-CoV-2 infection, mock means mock infection (Vero cell supernatant), untr means untreated, i.e. no treatment at all

polyA RNA-seq datasets

Caco-2 cells

time points	conditions
4h	untreated, mock, SARS-CoV-1, SARS-CoV-2
12h	SARS-CoV-1, SARS-CoV-2
24h	mock, SARS-CoV-1, SARS-CoV-2

H1299 cells

Note: these samples were harvested in parallel with the scRNA-seq and proteomics

time points	conditions
4h	untreated, mock, SARS-CoV-1, SARS-CoV-2
12h	SARS-CoV-1, SARS-CoV-2
24h	SARS-CoV-1, SARS-CoV-2
36h	mock, SARS-CoV-1, SARS-CoV-2

Calu-3 cells series 1

Note: the same RNA was used to prepare the totalRNA and smallRNA data mentioned below. Cells that were detached after 24h were collected from the supernatant by centrifugation and processed separately.

time points	conditions
4h	untreated, mock, SARS-CoV-1, SARS-CoV-2
12h	SARS-CoV-1, SARS-CoV-2
24h	mock, SARS-CoV-1, SARS-CoV-2
24h	detached cells from SARS-CoV-1 and SARS-CoV-2

Calu-3 cells series 2

Note: the same RNA was used to prepare the totalRNA and smallRNA data mentioned below. Cells that were detached after 24h were collected from the supernatant by centrifugation and processed separately.

time points	conditions
4h	mock, SARS-CoV-1, SARS-CoV-2
8h	SARS-CoV-1, SARS-CoV-2
12h	mock, SARS-CoV-1, SARS-CoV-2

Total RNA-seq dataset (rRNA depletion)

Calu-3

Note: the same RNA was used to prepare the polyA RNA series 1 and smallRNA data

time points	conditions
4h	untreated, mock, SARS-CoV-1, SARS-CoV-2
12h	SARS-CoV-1, SARS-CoV-2
24h	mock, SARS-CoV-1, SARS-CoV-2

SmallRNA-seq dataset

Calu-3

Note: the same RNA was used to prepare the polyA series 1 and smallRNA data

time points	conditions
4h	untreated, mock, SARS-CoV-1, SARS-CoV-2
12h	SARS-CoV-1, SARS-CoV-2
24h	mock, SARS-CoV-1, SARS-CoV-2

Single-cell RNA-seq datasets

H1299 cells

Note: these samples were harvested in parallel with the polyA RNA-seq and proteomics. Count table is provided for cells with more than 2000 detected genes.

time points	conditions
4h	mock
12h	SARS-CoV-1, SARS-CoV-2
24h	SARS-CoV-1, SARS-CoV-2
36h	mock, SARS-CoV-1, SARS-CoV-2

Calu-3 cells

Note: Count table is provided for cells with more than 1000 detected genes, however the analysis in the manuscript was done only with cells with more than 2000 detected genes.

time points	conditions
4h	mock, SARS-CoV-1, SARS-CoV-2
8h	SARS-CoV-1, SARS-CoV-2
12h	mock, SARS-CoV-1, SARS-CoV-2

Proteomics

H1299 cells

Note: these samples were harvested in parallel with the scRNA-seq and polyA RNA-seq

time points	conditions
4h	mock
12h	SARS-CoV-1, SARS-CoV-2
24h	SARS-CoV-1, SARS-CoV-2
36h	mock, SARS-CoV-1, SARS-CoV-2

Table S2, Related to Figure 1

Percentage of virals read in the data presented here and a previously published dataset (GEO identifier GSE147507, only human samples)

polyA RNA-seq datasets							
Caco-2 cells	% virus	**H1299 cells**	% virus	**Calu-3 cells series 1**	% virus	**Calu-3 cells series 2**	% virus
SARSCoV1-12h-A	26.53%	SARSCoV1-12h-A	0.09%	SARSCoV1-12h-A	35.79%	12h-SARSCoV1-1	5.00%
SARSCoV1-12h-B	27.18%	SARSCoV1-12h-B	0.12%	SARSCoV1-12h-B	38.17%	12h-SARSCoV1-2	5.40%
SARSCoV1-24h-A	35.67%	SARSCoV1-24h-A	0.13%	SARSCoV1-24h-A	48.13%	4h-SARSCoV1-1	0.33%
SARSCoV1-24h-B	34.60%	SARSCoV1-24h-B	0.14%	SARSCoV1-24h-A-sup	44.98%	4h-SARSCoV1-2	0.96%
SARSCoV1-4h-A	0.16%	SARSCoV1-36h-A	0.13%	SARSCoV1-24h-B	47.72%	8h-SARSCoV1-1	2.25%
SARSCoV1-4h-B	0.18%	SARSCoV1-36h-B	0.15%	SARSCoV1-24h-B-sup	51.72%	8h-SARSCoV1-2	3.10%
		SARSCoV1-4h-A	0.02%	SARSCoV1-4h-A	0.59%		
		SARSCoV1-4h-B	0.02%	SARSCoV1-4h-B	0.72%		
SARSCoV2-12h-A	10.96%	SARSCoV2-12h-A	0.06%	SARSCoV2-12h-A	32.89%	12h-SARSCoV2-1	35.77%
SARSCoV2-12h-B	12.80%	SARSCoV2-12h-B	0.05%	SARSCoV2-12h-B	32.97%	12h-SARSCoV2-2	39.63%
SARSCoV2-24h-A	22.39%	SARSCoV2-24h-A	0.04%	SARSCoV2-24h-A	16.48%	4h-SARSCoV2-1	1.58%
SARSCoV2-24h-B	22.69%	SARSCoV2-24h-B	0.04%	SARSCoV2-24h-A-sup	25.02%	4h-SARSCoV2-2	1.62%
SARSCoV2-4h-A	0.08%	SARSCoV2-36h-A	0.04%	SARSCoV2-24h-B	12.69%	8h-SARSCoV2-1	16.12%
SARSCoV2-4h-B	0.10%	SARSCoV2-36h-B	0.04%	SARSCoV2-24h-B-sup	16.18%	8h-SARSCoV2-2	15.16%
		SARSCoV2-4h-A	0.01%	SARSCoV2-4h-A	1.75%		
		SARSCoV2-4h-B	0.01%	SARSCoV2-4h-B	2.02%		

Total RNA-seq dataset (rRNA depletion)	
Calu-3	
Note: the same RNA was used to prepare the polyA RNA series 1 and smallRNA data	
	% virus
SARSCoV1-12h-A	56.81%
SARSCoV1-12h-B	58.68%
SARSCoV1-24h-A	76.72%
SARSCoV1-24h-B	77.10%
SARSCoV1-4h-A	1.13%
SARSCoV1-4h-B	1.95%
SARSCoV2-12h-A	54.23%
SARSCoV2-12h-B	54.30%
SARSCoV2-24h-A	48.18%
SARSCoV2-24h-B	42.87%
SARSCoV2-4h-A	2.55%
SARSCoV2-4h-B	3.01%

GSE147507 samples	MOI of 0.2 for 24 h
Sample	% virus
Series15_COVID19Lung_1	0.00006%
Series15_COVID19Lung_2	0.002%
Series1_NHBE_SARS-CoV-2_1	0.10%
Series1_NHBE_SARS-CoV-2_2	0.08%
Series1_NHBE_SARS-CoV-2_3	0.10%
Series2_A549_SARS-CoV-2_1	0.03%
Series2_A549_SARS-CoV-2_2	0.03%
Series2_A549_SARS-CoV-2_3	0.03%
Series5_A549_SARS-CoV-2_1	0.08%
Series5_A549_SARS-CoV-2_2	0.08%
Series5_A549_SARS-CoV-2_3	0.11%
Series6_A549-ACE2_SARS-CoV	53.60%
Series6_A549-ACE2_SARS-CoV	49.83%
Series6_A549-ACE2_SARS-CoV	57.49%
Series7_Calu3_SARS-CoV-2_1	13.19%
Series7_Calu3_SARS-CoV-2_2	17.01%
Series7_Calu3_SARS-CoV-2_3	14.58%

Table S3, Related to Figure 1

(provided as Excel Table)

Table S4, Related to Figure 4

Statistics scRNA-seq

H1299

						(more than 1 raw viral read count)		
						no virus	with S1	with S2
H1299-mock-4h-A	696	695	1	0	H1299-mock-	99,86%	0,14%	0,00%
H1299-mock-4h-B	647	645	2	0	H1299-mock-	99,69%	0,31%	0,00%
H1299-mock-36h-A	1924	1924	0	0	H1299-mock-	100,00%	0,00%	0,00%
H1299-mock-36h-B	1081	1081	0	0	H1299-mock-	100,00%	0,00%	0,00%
H1299-S1-12h-A	2354	944	1410	0	H1299-S1-12	40,10%	59,90%	0,00%
H1299-S1-12h-B	1665	515	1150	0	H1299-S1-12	30,93%	69,07%	0,00%
H1299-S1-24h-A	1050	287	763	0	H1299-S1-24	27,33%	72,67%	0,00%
H1299-S1-24h-B	1787	359	1428	0	H1299-S1-24	20,09%	79,91%	0,00%
H1299-S1-36h-A	3005	843	2162	0	H1299-S1-36	28,05%	71,95%	0,00%
H1299-S1-36h-B	793	596	197	0	H1299-S1-36	75,16%	24,84%	0,00%
H1299-S2-12h-A	1985	1586	0	399	H1299-S2-12	79,90%	0,00%	20,10%
H1299-S2-12h-B	1710	894	0	816	H1299-S2-12	52,28%	0,00%	47,72%
H1299-S2-24h-A	1363	976	0	387	H1299-S2-24	71,61%	0,00%	28,39%
H1299-S2-24h-B	1227	1118	0	109	H1299-S2-24	91,12%	0,00%	8,88%
H1299-S2-36h-A	2162	1577	0	585	H1299-S2-36	72,94%	0,00%	27,06%
H1299-S2-36h-B	1305	1217	0	88	H1299-S2-36	93,26%	0,00%	6,74%

Calu-3

						(more than 3 raw viral read counts)		
						no virus	with S1	with S2
Calu3-mock-4h-A	1454	1451	3	0	Calu3-mock-	99,79%	0,21%	0,00%
Calu3-mock-4h-B	839	838	0	1	Calu3-mock-	99,88%	0,00%	0,12%
Calu3-mock-12h-A	1074	1074	0	0	Calu3-mock-	100,00%	0,00%	0,00%
Calu3-mock-12h-B	732	728	0	4	Calu3-mock-	99,45%	0,00%	0,55%
Calu3-S1-4h-A	642	226	416	0	Calu3-S1-4h-	35,20%	64,80%	0,00%
Calu3-S1-4h-B	654	251	403	0	Calu3-S1-4h-	38,38%	61,62%	0,00%
Calu3-S1-8h-A	1428	0	1428	0	Calu3-S1-8h-	0,00%	100,00%	0,00%
Calu3-S1-8h-B	970	0	970	0	Calu3-S1-8h-	0,00%	100,00%	0,00%
Calu3-S1-12h-A	715	0	715	0	Calu3-S1-12h	0,00%	100,00%	0,00%
Calu3-S1-12h-B	807	0	807	0	Calu3-S1-12h	0,00%	100,00%	0,00%
Calu3-S2-4h-A	551	355	0	196	Calu3-S2-4h-	64,43%	0,00%	35,57%
Calu3-S2-4h-B	1170	736	0	434	Calu3-S2-4h-	62,91%	0,00%	37,09%
Calu3-S2-8h-A	948	0	0	948	Calu3-S2-8h-	0,00%	0,00%	100,00%
Calu3-S2-8h-B	510	0	0	510	Calu3-S2-8h-	0,00%	0,00%	100,00%
Calu3-S2-12h-A	767	0	0	767	Calu3-S2-12h	0,00%	0,00%	100,00%
Calu3-S2-12h-B	732	0	0	732	Calu3-S2-12h	0,00%	0,00%	100,00%

Transparent Methods

Cell culture

Vero E6 (ATCC CRL-1586), Calu-3 (ATCC HTB-55), Caco-2 (ATCC HTB-37) and H1299 (ATCC CRL-5803) were cultivated in Dulbecco's modified Eagle's medium (DMEM) supplemented with 10% heat-inactivated fetal calf serum, 1% non-essential amino acids, 1% L-glutamine and 1% sodium pyruvate (all Thermo Fisher Scientific) in a 5% CO_2 atmosphere at 37 °C.

Poly-I:C transfections

Transient transfection of eukaryotic cells was performed using X-tremeGENE™ siRNA transfection reagent (Roche) according to the manufacturer´s instructions. Briefly, 2x10^5 cells/ml were grown in 6-well plates for 24 h and fresh DMEM without antibiotics was added. OptiPRO SFM™ (Gibco) was supplemented with 0.25 µg poly(I:C) (Invivogen) and 0.75 µl X-tremeGENE™ siRNA reagent, incubated for 15 min, and 100 µl transfection mix was added to the cells.

RT-qPCR on intracellular RNA

RNA was isolated from Trizol using the RNA clean and concentrator kit (Zymo). The RNA was reverse transcribed using maxima RT and subjected to qPCR as described (Wyler et al., 2019). Primers used for qPCR are listed in supplementary table 5.

Viruses

SARS-CoV (Frankfurt strain, NCBI accession number AY310120) and SARS-CoV-2 (Patient isolate, BetaCoV/Munich/BavPat1/2020|EPI_ISL_406862) were used. For virus stock production, virus was grown on Vero E6 cells and concentrated using Vivaspin® 20 concentrators (Sartorius Stedim Biotech). Virus stocks were stored at -80°C, diluted in OptiPro serum-free medium supplemented with 0.5% gelatine (Sigma Aldrich) and phosphate-bufferd saline (PBS, Thermo Fisher Scientific). Titer was defined by plaque titration assay. Cells inoculated with cell culture supernatants from uninfected Vero cells mixed with OptiPro serum-free medium supplemented with 0.5% gelatine and PBS, in accordance to virus stock preparation, serves as mock infected controls. All infection experiments were carried out under biosafety level three conditions with enhanced respiratory personal protection equipment.

Virus growth kinetics and plaque titration assay

24 h prior to infection, the different cell lines were seeded to 70% confluence. The cells were washed once with PBS before virus (diluted in OptiPro serum-free medium) adsorption. After

incubation for 1 h at 37 °C, 5% CO2 the virus-containing supernatant was discarded and cells were washed twice with PBS and supplied with DMEM as described above.

To determine the amount of infectious virus particles in the supernatant a plaque titration assay was performed. For the assay Vero E6 cells were seeded to confluence and infected with serial dilution of virus-containing cell culture supernatant diluted in OptiPro serum-free medium. One hour after adsorption, supernatants were removed and cells overlaid with 2.4% Avicel (FMC BioPolymers) mixed 1:1 in 2xDMEM. Three days post-infection the overlay was removed, and cells were fixed in 6% formaldehyde and stained with a 0.2% crystal violet, 2% ethanol and 10% formaldehyde.

Western Blot Analysis

The expression of human ACE-2 (hACE-2) was confirmed by Western blot analysis. For the preparation of total cell lysate cells were washed with PBS and lysed in RIPA Lysis Buffer (Thermo Fisher Scientific) supplied with 1% Protease Inhibitor Cocktail Set III (Merck Chemicals). After an incubation of 30 min at 4 °C, cell debris were pelleted (10 min, 13,000 x g, 4 °C) and the supernatant transferred to a fresh reaction tube. For determining protein concentration Thermo Scientific's Pierce™ BCA Protein Assay Kit, according to the manufacturer's instructions was used. The protein lysates were mixed with 4xNuPAGE LDS Sample Buffer (Invitrogen) supplemented with 10% 2-mercaptoethanol (Roth). Protein lysates were separated by size on a 12% sodium dodecyl sulfatepolyacrylamid (SDS) gel and blotted onto a 0.2 µm polyvinylidene difluoride (PVDF) membrane (Thermo Scientific) by semi-dry blotting (BioRad). Primary detection of hACE-2 was done using a goat anti-hACE-2 antibody (1:1,250; #AF933, R&D Systems), a horseradish peroxidase (HRP)-labeled donkey anti-goat antibody (1:5,000, Dianova) and Super Signal West Femto Chemiluminescence Substrate (Thermo Fisher Scientific). As loading control, samples were analyzed for β-actin expression using a mouse anti-β-actin antibody (1:5,000, Sigma Aldrich) and a HRP-labeled goat anti-mouse antibody (1:10,000, Sigma-Aldrich).

Infections for RNA sequencing experiments

Calu-3 cells and H1299 cells were seeded at a concentration of 6 x 10^5 cells/mL and 5 x 10^4 cells/mL, respectively. 24 h post seeding cells were infected with SARS-CoV and SARS-CoV-2 at an MOI of 0.33 or Vero cell supernatant mixed with OptiPro serum-free medium supplemented with 0.5 % gelatine and PBS as negative control. 4, 8, 12 and 24 hpi samples were taken. For sequencing of total RNA the supernatant was removed and Trizol LS Reagent (Thermo Fisher Scientific) was applied to the cell-layer and incubated for 1 min at room temperature until the cells were lysed. The suspension was then transferred to a RNase

free reaction tube (Thermo Fisher Scientific) and stored at -80 °C. For scRNA-seq sample preparation the cells were washed with pre-warmed PBS, detached with pre-warmed trypsin for 3 min at 37 °C. The detached cells were transferred into a reaction tube (Eppendorf) and the following steps were performed on ice. Cells were spinned down at 1000 x g for 2 min at 4 °C, resuspended in PBS properly and passed through a 35 µm blue snap cap cell strainer (STEMCELL) and again pelletized The cell pellet was then resuspended in pre-chilled methanol (Roth) and stored at -80 °C.

RNA sequencing

Poly-A RNA sequencing

Poly-A RNA sequencing libraries were prepared using the NEBNext Ultra II Directional RNA Library Prep Kit (NEB) according to the manufacturer's protocols. Libraries were sequenced on a NextSeq 500 device at 1x76 cycles.

Small RNA sequencing

100 ng of total RNA of each condition was used for small RNA library preparation. Library preparation was performed using the SMARTer smRNA-Seq kit for Illumina from Clontech according to manufacturer's instruction. The small RNA libraries were pooled together with 19 % PhiX and sequenced on the NextSeq 500, 1 x 50 cycles.

Total RNA sequencing

1 µg of total RNA of each condition was used for total RNA library preparation. First, samples were depleted of ribosomal RNA using the RiboCop rRNA Depletion Kit (Lexogen) according to manufacturer's instruction. Following, ribo-depleted samples were processed with the TruSeq mRNA stranded kit from Illumina according to manufacturer's instruction. The total RNA libraries were sequenced on the HiSeq 4000, 2 x 76 cycles.

Viral RNA-seq analysis

Total and poly(A)$^+$ RNA-seq reads were mapped with STAR 2.7.3a to a combined genome comprised of GRCh38 and GenBank MN908947 (SARS-CoV-2) or AY310120 (SARS-CoV) using permissive parameters for noncanonical splicing [36, 101]. Viral genes were quantified by taking the top eight noncanonical splice events called by STAR across all total RNA-seq datasets according to the numbers of uniquely-mapping reads spanning the junction (Supplemental Table 3; note that for host cell gene expression analysis, also non-uniquely mapped reads were used). To estimate levels of ORF1ab, insertions, soft-clipping events and split reads were filtered from virus-mapping reads, followed by intersection with positions 53-83 of the virus using bedtools, requiring a minimum of 24 nucleotides overlap to reflect the parameters STAR requires to call a noncanonical splice junction [102]. These counts were either

combined with a count matrix of the human genes quantified by STAR and TMM/CPM normalized with edgeR (Figure S1D) or normalized by the total number of viral junction-spanning reads per time point (Figure S1E) [103]. Coverage plots were made from merged STAR-mapped BAM files, or from Bowtie-mapped small RNA-seq BAM files using ggsashimi [104]. This workflow was implemented with custom Python scripts in a Snakemake pipeline [105].

microRNA analysis

Raw reads were preprocessed by trimming with cutadapt (version 2.9) in two passes, first trimming i) the Illumina TruSeq adaptor at the 3' end and allowing for one mismatch,
ii) all 3'end bases with mean Phred score below 30 and iii) the three 5'end overhang nucleotides associated with the template-switching Clontech library preparation protocol.
In the second pass, poly(A)-tails were trimmed. Trimmed reads were mapped using bowtie (version 1.2.2) to a SARS genome consisting of the combined SARS-CoV and
SARS-CoV-2 genomes using the non-standard parameters (-q -n 1 -e 80 -l 18 -a -m 5 –best –strata). Reads that did not align to the SARS-CoV genome were aligned to the
GRCh38 genome. The expression of known miRNAs (miRBase 22 annotation) was estimated using mirdeep2 (version 2.0.0.7) and standard parameters.
The differential expression analysis used the limma [106] and edgeR [103] packages after applying the voom transformation to the TMM-normalized count data produced by mirdeep2.
For the different viral infections we contrasted SARS-CoV-2 24 h / SARS-CoV-2 4 h with mock 24 h / mock-4 h in order to test for those miRNAs differentially expressed long after the infection having removed any effects seen in mock as well.

TaqMan assays

TaqMan probes were purchased from ThermoFisher. 10 ng to 50 ng of total RNA were used for TaqMan assays and assays were performed according manufacturer's instruction with minor modifications. The minor modifications were: 10 mM dNTPs, Superscript III, 5 x FS buffer and Ribolock were used for the reverse transcription (RT) reaction and for 50 ng RNA input only 2 µl of the RT primer was used. All biological samples were handled in triplicates and the Ct values were normalized to the let-7a control.

Northern Blot

2,5 µg to 5 µg of total RNA were mixed equally with 2 x RNA loading dye, following denaturation for 5 min at 95 °C. The RNA of the denaturated samples was separated on 15 % urea polyacrylamide gels, transferred onto Hybond-N+ nylon membranes, UV crosslinked at 120.000 µJ/cm2 and probed with double digoxigenin (DIG)-labeled locked nucleic acid (LNA) detection probes (Qiagen, see supplementary table 5) at 55 °C over-night. The membranes were

subjected to stringent washes using SSC/SDS buffers. Subsequently, membranes were incubated with an anti-DIG-alkaline phosphatase (AP) solution (1:2500 diluted in blocking solution (Roche)) for 30 min at room temperature. Finally, northern blot signals were visualized using CDP star reagent (Roche) and the Vilber Fusion FX system according to manufacturer's instructions. The northern blot signals were normalized to the band intensity of the let-7a loading control.

Bulk RNA-sequencing analysis using DESeq2

Starting from count tables, RNA sequencing results were analysed on a per run basis comparing infected samples to time matched mock experiments unless otherwise specified using DESeq2 [107] version 1.22.2. Genes with a maximum read count across samples of less than two were filtered out. Differentially expressed genes were defined as genes with an absolute fold change in mRNA abundance greater than 1.5 ($\log_2$ fold change of 0.58 - using DESeq2 shrunken $\log_2$ fold changes) and an adjusted p-value of less than 0.05 (Benjamini-Hochberg corrected).

Gene ontology and KEGG enrichment analysis.

Genes whose mRNAs were found to be differentially expressed were subjected to gene set overrepresentation analysis using the clusterProfiler package in R [108].

Single-cell RNA-seq

Methanol-fixed cells were centrifuged at 2,000 x g for 5 min, rehydrated in 1 mL rehydration buffer containing 0.01% PBS/BSA and 1:100 Superasein (Thermo Fisher), and resuspended in 400 µL rehydration buffer followed by passing through a 40 µm cell strainer. Encapsulation was done with the Nadia system (Dolomite biosystems) using the built-in standard procedure. For library preparation, we followed the version 1.8 of the manufacturer's protocol, which is based on the protocol established by [109], with adding a second-strand synthesis step [110].

For the encapsulation, 75,000 cells in 250 µL rehydration buffer were used, with 250 µL of lysis buffer (6% Ficoll PM-400, 0.2% Sarkosyl, 20 mM EDTA, 200 mM Tris pH 7.5, 50 mM DTT) and 3 mL oil (Biorad #1864006). After encapsulation, beads were recovered from the emulsion by washing with 2 x 30 mL 6 x saline sodium citrate buffer (diluted from Sigma #S6639) buffer in a 5 µm ÜberStrainer (pluriSelect). After another washing step in 1.5 mL 6 x SSC, cells were washed with 5 x reverse transcription buffer (250 mM Tris pH 8, 375 mM KCl, 15 mM MgCl2, 50 mM DTT) and resuspended in 200 µL RT mix (50 mM Tris pH 8, 75 mM MgCl2, 3 mM MgCl2, 10 mM DTT, 4% Ficoll PM-400, 1 mM each dNTPs, 2.5 µM Macosko TSO, 10 µl Maxima H- RT enzyme). Beads were incubated for 30 min at room temperature and 90 min at 42 °C (all incubation steps on a rotator). After washing once with TE/0.5% SDS and twice with TE/0.01% Tween, beads were incubated in 200 µL exonuclease

mix (10µl Exonuclease in 1xexonuclease buffer, NEB #M0293) for 45 min at 37 °C, again on a rotator. After washing with once with TE/0.5% SDS and twice TE/0.01% Tween, beads were incubated for 5 min in 0.1 M NaOH, washed with TE/0.01% Tween and TE, and incubated in 200 µl second strand mix (50 mM Tris pH 8, 75 mM MgCl2, 3 mM MgCl2, 10 mM DTT, 12% PEG 8000, 1 mM each dNTPs, 10 µM dN-SMRT oligo, 5 µl Klenow enzyme NEB #M0212) for 1 h at 37 °C. Beads were again washed in TE/0.01% Tween and stored overnight in TE/0.01% Tween, then washed in TE and twice in water, and per sample eight PCR reactions with 4,000 beads each in 50µl using 1µM SMART PCR primer (oligos in supplementary table 5) and the 2x Kapa HiFi Hotstart Ready mix (Roche #07958935001) were performed, with pre-incubation for 3 minutes at 95 °C, then 4 cycles 98 °C/20s, 65°C/45s, 72 °C/3min, then 9 cycles 98 °C/20s, 67°C/20s, 72 °C/3min, then post-incubation for 3 minutes at 72 °C. The eight PCR reaction were pooled in three clean-up reactions using Ampure XP beads. For each oft the three sub-samples, a Nextera XT v2 (Illumina) reaction was performed with 600 pg DNA. In a 20µl reaction, 10 µl tagment DNA buffer and 5 µl amplicon tagment mix were incubated for 5 minutes at 55 °C, and, after addition of 5 µl neutralization buffer for 5 minutes at room temperature. Afterwards, 15 µl PCR master mix were added, 200 nM New-P5-SMART PCR hybrid oligo, 200 nM index oligo in total 50 µl. The Nextera reactions were then again pooled, purified using Ampure XP beads, and sequenced on a NovaSeq 6000 deviced with 21+71 cycles using Read1CustomSeqB for read 1.

Single-cell data analysis

After trimming one nucleotide from the 3' end of read one, count tables were generated using the PiGx-scRNA-seq pipeline [111] version 1.1.4. In short, cells are separated from empty barcodes using the inflection method as implemented in the dropbead package [112]. The reads are then mapped to the combined human and viral genome using the STAR aligner [101], with the default parameters. The resulting spliced and unspliced digital expression matrices are converted into loom, Seurat and SingleCellExperiment formats. For read mapping to the viral genomes, we used for SARS-CoV, the Frankfurt strain genome (accession number AY310120) and for SARS-CoV-2 the original Wuhan sequence (accession number MN908947.3). For both viruses, a feature labelled "UTR3" was added between the last annotated gene and the 3'-end, which captured most of the reads. Since the genes were counted separately, the scRNA-seq data contains counts for all genes in the annotation. Preprocessing was done in R (version 3.6), using the Seurat package [84]. Cells with less than 2000 unspliced reads were filtered out of the analysis. Raw reads were then normalized, and scaled. Variable genes were defined using the variance

stabilizing method. Dimensionality reduction was performed using diffusion maps, as implemented in the destiny Bioconductor [64] package.

Diffusion components were used as the basis for UMAP embeddings [113]. Pseudotime inference was performed using the diffusion pseudotime trajectory [65]. A secondary UMAP embedding was constructed by using, as input, the diffusion pseudotime calculated probabilities of cell-cell transitions. The UMAP was embedded using the python package umap-learn. All processing was done using the default parameters. The processing was done separately both with and without including SARS-CoV and SARS-CoV-2 viral genes. Viral load was calculated as the sum of detected viral reads in each cell. Velocity estimation was performed using the R implementation of the original Velocyto method [62]. The following parameters were used for the projection of the vector field: n = 200, scale = 'sqrt', arrow.scale = 3, min.grid.cell.mass = 0.5.

To increase the power of detecting dynamic changes in gene expression (Fig. 5E), pseudotime based embedding was dynamically discretized using the Louvain algorithm. The input to the Louvain algorithm are eigenvectors of the diffusion matrix. The resulting bins were ordered based on the median SARS-CoV-2 expression, and the percentage of cells expressing genes of interest was visualized in each of the bins. The ordering of bins based on the median SARS-CoV-2 load corresponded almost exactly to the velocyto inferred trajectories.

Both Calu3 and H1299 cells were analyzed using the same parameters. To detect changes happening early in infection, Calu3 4h cells were additionally separately analyzed.

Preprocessing and analysis/figure scripts are available at github (https://github.com/BIMSBbioinfo/Ewyler_SARS-CoV).

The analysis was visualized using ggplot2 [114], ggrepel [115], and the interactive exploration was enabled by iSEE [116].

HSP90 inhibitor experiments

The HSP90 inhibitors were purchased either from Sigma (17-AAG, A8476) or from Selleckchem (Onalespib, S1163 and Ganetespib, S1159), and dissolved in DMSO. Cells were seeded and grown to subconfluence and infected with SARS-CoV-2 MOI 0.01 (Calu-3) or MOI 0.5 (AECs) diluted in OptiPro serum free medium. After 1 h virus adsorption the supernatant was removed and cells were washed twice with PBS. DMEM containing dilutions of 17-AAG (200 nM, 400 nM, 800 nM, 2,000 nM) or DMSO as solving control. Samples for detection of viral RNA and infectious particles in the supernatant as well as total RNA within the cells were taken 8, 16 and 24 hpi.

The cytotoxicity of the the HSP90 inhibitor was assured by cell viability assay using CellTiter-Glo® Luminescent Cell Viability Assay according to manufacturer's instruction (Promega). The activity of untreated cells was set as 100% and cells were treated with different concentrations of 17-AAG. The viability of cells was measured 16 and 24 h after treatment using Mithras Luminescence microplate reader (Berthold).

Primary airway epithelial cells

Cells isolated from distal lung tissue were cultured as described in Imai-Matsushima et al., 2018. Briefly, for expansion primary cells were co-cultivated with gamma-irradiated mitotically inactivated NIH3T3 mouse embryonic fibroblasts (MEFs) in a 3:1 mixture of Ham's F-12 nutrient mix (Life technologies) and DMEM supplemented with 5% FCS, 0.4µg/mL hydrocortisone (Sigma-Aldrich), 5µg/mL recombinant human insulin (Sigma-Aldrich), 8.4 ng/mL cholera toxin (Sigma-Aldrich), 24µg/mL Adenine (Sigma-Aldrich), and 10ng/mL recombinant human epidermal growth factor (Invitrogen), 0.1 µM DBZ (Tocris) and 9 µM Y27632 (Miltenyi Biotec)

Differentiation was induced by additional treatment with 3 µM CHIR-99021 (Sigma), 10 ng/ml KGF (Invitrogen), 10 ng/ml FGF-10 (Invitrogen), 100 µM IBMX (Sigma), 100 µM 8-Bromoadenosine 3',5'-cyclic monophosphate (Biolog), 25 nM Dexamethason (Sigma) and 20 µM DBZ for 3 days. Two days prior to infection the primary cells were separated from the MEFs by differential trypsinization and subsequently seeded in cell culture vessels in DMEM with 10% FCS, 1% non-essential amino acids, 1%, L-glutamine and 1% sodium pyruvate.

RT-qPCR of viral RNA in the supernatant

The viral RNA from supernatant of infected cells was isolated using the NucleoSpin RNA virus isolation kit (Macherey-Nagel) according to the manufacturer's instructions. To determine the amount of viral genome equivalents the previously published assay specific for both SARS-CoV and SARS-CoV-2 Envelope gene [117] was used. Data analysis was done using LightCycler Software 4.1 (Roche).